

Kinetic Equilibrium Prediction at TCV using RAPTOR and FBT

C. E. Contré¹, A. Merle¹, O. Sauter¹, S. Van Mulders^{1,2}, R. Coosemans¹, G. Durr-Legoupil-Nicoud¹, F. Felici¹, O. Février¹, C. Heiss¹, B. Labit¹, A. Pau¹, Y. Poels^{1,3}, C. Venturini¹, B. Vincent¹, the TCV team⁴, and the EUROfusion Tokamak Exploitation Team⁵

¹Ecole Polytechnique Fédérale de Lausanne (EPFL), Swiss Plasma Center (SPC), CH-1015 Lausanne, Switzerland

²ITER Organization, Route de Vinon sur Verdon, St Paul Lez Durance, 13115, France

³Present address: Google DeepMind, London, UK

⁴See author list of B. P. Duval et al. 2024 Nucl. Fusion 64 112023

⁵See author list of E. Joffrin et al. 2024 Nucl. Fusion 64 112019

E-mail: cassandre.contre@epfl.ch

Keywords: RAPTOR, FBT, KEP, Equilibrium, Transport, Predict-first, TCV

Abstract

We present results from a new Kinetic-Equilibrium Prediction (KEP) workflow and shot preparation for full TCV discharges, by coupling predict-first RAPTOR transport simulations with FBT inverse equilibrium calculations. RAPTOR is a 1.5D transport code which has been extensively used for plasma shot optimization and real-time modeling. We show that rapid pre-shot simulations can be performed directly using information from the pulse schedule across a wide range of plasma shapes and scenarios, given an estimate of the confinement quality factor $H^{98(y,2)}$ and line-averaged density. The resulting p' and TT' profiles are then provided to the pre-shot equilibrium computation performed by FBT — a static free-boundary solver routinely used at TCV — achieving convergence between the two codes in a few iterations. Finally, we show that this coupling, when integrated into the TCV shot preparation, improves the evaluation of the coil currents needed to match the target plasma shape; in particular providing an accurate estimate of critical quantities such as the internal inductance l_i and normalized pressure β_N , giving more realistic information to tokamak operators about the expected pulse behavior and enabling them to adjust the plan correspondingly.

1 Introduction

Any attempt to optimize tokamak performance is inevitably confronted to operational limits, beyond which machine protection systems or disruptions may prematurely terminate a pulse [1]. Most of the 0D limits known to date to prevent these events have been formalized since decades [2, 3], although regularly refined [4], and are now increasingly compared with results from integrated pulse simulation workflows, to assess scenario feasibility in light of the full non-linear spatial and temporal dynamics of a plasma discharge. In particular, pulse design and optimization tools, able to simulate, optimize and prepare a scenario shortly before an experiment [5–8], and flight simulators, which integrates the response of the actuators to the control system [9], are two complementary tools used in shot preparation which demand to simulate a whole plasma discharge, from ramp-up to ramp-down, with reasonable computational time. Modeling scenarios with these tools will be a prerequisite for conducting experiments on next step devices like ITER [2], while smaller tokamaks like the *Tokamak à Configuration Variable* (TCV) [10] can be used for testing and validation. In this paper, we present the development of a predict-first pulse planning workflow in which RAPTOR [11] is used to predict the self-consistent response of the current density, elec-

tron and ion temperatures, and particle density profiles to actuators, while providing these profiles to FBT [12] for computing the equilibrium and coil currents required to sustain the desired shape and position. RAPTOR is a rapid solver of the 1D radial transport equations in the plasma core. It is implemented in MATLAB with the ability to automatically generate code in C, for accelerating computations or integration in real-time control systems, for example in TCV [11, 13, 14], RFX [15], JET [16] and ASDEX-Upgrade [17, 18]. Previous works also demonstrated its ability to optimize scenarios [19–23] and to integrate new physics models, such as the Qualikiz surrogate model, QLKNN-10D [20, 24]. However, its ability to predict transport rapidly and automatically before an experiment remained to be demonstrated. By using the gradient-based transport model [19, 25] together with the Martin scaling law [26] for predicting the L- to H-mode transition times, this work investigates the extent to which it is possible to predict with RAPTOR the evolution of the kinetic and current density profiles, including the evolution of the poloidal beta β_{pol} and internal inductance l_i , from the current ramp-up to ramp-down, purely based on information available before the shot. We will also show, in particular, that estimating the line-averaged density ($n_{e,l}$) from the gas programming remains a del-

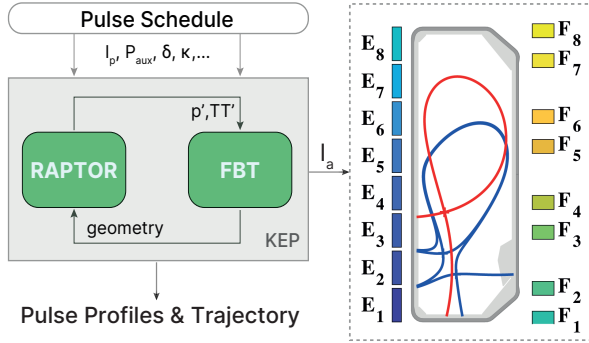


Figure 1: Schematic overview of the Kinetic Equilibrium Prediction (KEP) workflow. The pulse schedule is given as input to RAPTOR and FBT, loosely coupled to provide the active coil currents and pulse profiles predictively. These new feedforward currents traces are then integrated into the TCV preparation system to control the plasma shape and position with its 16 separately powered PF coils. Examples of #82030 (lower single-null, LSN, in red) and #83575 (snowflake (SF) upper NT, in blue) shapes, achievable at TCV and simulated with the KEP (see Sec. 4), are also represented.

icate and essential step towards predicting the kinetic profiles before the discharge, and would need further investigation. Similarly, improving our ability to predict L-H/H-L transitions for various scenarios is also an important step. This rapid prediction of the current diffusion and heat and particle transport in the plasma core aims to inform scientific coordinators on the evolution of key physical quantities for scenario planning, but also to inform other modeling tools.

Predicting the plasma pressure and current density with RAPTOR can indeed help to improve the correctness of the equilibrium used for designing the poloidal field (PF) coil currents by providing an estimate of the pressure gradient $p'(\psi, t)$ and current function $TT'(\psi, t)$ ($T = RB_\phi$) time evolution. How to provide realistic internal profiles to equilibrium calculations is a longstanding challenge. In reconstruction codes, like LIUQE [27], this problem can be solved by constraining the profiles with experimental measurements and modeling. This coupling method, called Kinetic Equilibrium Reconstruction (KER), has already been demonstrated with RAPTOR and LIUQE for real-time and post-shot reconstruction in [14] and [28], as also done in the ASTRA-LIUQE KER [29], CLISTE [30], IDE [31, 32] and EFIT [33, 34]. In a similar way, preparing the equilibrium of a discharge for pulse planning purposes requires to make a prediction on profiles in the core. A natural solution is to couple the inverse equilibrium solver with the predict-first simulations of a transport solver, as discussed above. This strategy is defined here as KEP for Kinetic Equilibrium Prediction (or Preparation). In this

paper, we describe the coupling between FBT and RAPTOR, with a similar method to the one presented in [14] for the real-time RAPTOR-LIUQE KER. It will be shown that providing the predicted internal profiles to FBT enhances the calculation of the feedforward poloidal field (PF) coil currents (Fig. 1) required to maintain the magnetic topology, while the plasma evolves, reducing the risk of disruptions and plasma shape misalignment. At the time of writing, similar kinetic-equilibrium coupling [35] has been reported between FEEQS [36] and METIS [5] at JT-60SA, and is currently under development [37, 38] for SPARC with TORAX [39] and GSpulse [40].

The paper is structured as follow. Section 2 presents the KEP equations and methodology. Section 2.1 describes the RAPTOR model used for pre-shot simulations in TCV, including a new model for H-mode transition that extends the Martin scaling law [26] to favorable and unfavorable magnetic configurations. The gradient-based model, originally designed to cover transitions from L to H mode, has been extended to include changes in triangularity, accounting for the higher L-mode performances observed in Negative Triangularity (NT) [41–45]. Equations of the inverse equilibrium problem are reminded in Section 2.2, introducing the FBT-RAPTOR coupling in Section 2.3. The transport and equilibrium calculations are benchmarked on 211 shots in Section 3, statistically validating the models with various shapes and scenarios. Section 4 finally reports on the integration of the new coupling solution into the TCV shot preparation system. We discuss how this new preparation enhances the stability and accuracy of the equilibria, along with possible directions for improvement of the present approach.

2 Physics models and codes

2.1 RAPTOR

RAPTOR is a fast and light transport simulator for the current density (j_{\parallel}), temperatures ($T_{e,i}$) and electron density (n_e). In other words, it solves for a non-linear system of PDEs of the form¹:

$$\sigma_{\parallel} \frac{2\pi\hat{\rho}}{V'} \left(\frac{\partial}{\partial t} - \frac{\hat{\rho}\dot{\Phi}_B}{2\Phi_B} \frac{\partial}{\partial \hat{\rho}} \right) \psi = \underbrace{\frac{g_a}{\mu_0\hat{\rho}} \frac{\partial}{\partial \hat{\rho}} \left(\frac{g_b}{\hat{\rho}} \frac{\partial \psi}{\partial \hat{\rho}} \right)}_{\propto j_{\parallel, tot}} - (j_{bs} + j_{cd})$$

$$\frac{3}{2} (V')^{\frac{5}{3}} \left(\frac{\partial}{\partial t} - \frac{\hat{\rho}\dot{\Phi}_B}{2\Phi_B} \frac{\partial}{\partial \hat{\rho}} \right) [(V')^{-\frac{5}{3}} n_{e,i} T_{e,i}] + \frac{1}{V'} \frac{\partial}{\partial \hat{\rho}} \hat{Q}_{e,i} = P_{e,i},$$

$$\frac{1}{V'} \left(\frac{\partial}{\partial t} - \frac{\hat{\rho}\dot{\Phi}_B}{2\Phi_B} \frac{\partial}{\partial \hat{\rho}} \right) [V' n_e] - \frac{1}{V'} \frac{\partial}{\partial \hat{\rho}} \hat{\Gamma}_e = S_e,$$

using the normalised toroidal flux coordinate $\hat{\rho} = \sqrt{\frac{\Phi}{\Phi_B}}$, with ψ [Wb] being the magnetic poloidal flux, defined following the COCOS-11 convention [48], Φ [Wb] the enclosed toroidal flux, Φ_B its value at the plasma boundary, and given a set of flux-surface averaged current j_{cd} [A.m⁻²], power $P_{e,i}$ [W.m⁻²] and

¹More detailed formulations of these equations can be found in [11, 46, 47]

particle $S_e[\text{m}^{-3}.\text{s}^{-1}]$ source profiles. Information on the geometry is embedded in the non-dimensional coefficients $g_a = \frac{T^2}{16\pi^2\Phi_B^2}$ and $g_b = \langle \frac{1}{R^2} \rangle \langle \frac{(\nabla V)^2}{R^2} \rangle$, and in the volume radial derivative $V'_\rho = \frac{dV}{d\rho}[\text{m}^3]$, usually computed externally from an equilibrium code, where $\langle \cdot \rangle$ denotes flux-surface average, R the major radius, $T = RB_\phi$ with B_ϕ the toroidal magnetic field. We also define $V_\rho = \rho_B V'_\rho[\text{m}^2]$ the derivative with respect to the unnormalised toroidal radius, evaluated at the boundary as $\rho_B = \sqrt{\frac{\Phi_B}{\pi B_0}}$, and $Q_{e,i}[\text{W}.\text{m}^{-2}] = V_\rho^{-1} \hat{Q}_{e,i}[\text{W}]$ and $\Gamma_{e,i}[\text{m}^2.\text{s}^{-1}] = V_\rho^{-1} \hat{\Gamma}_{e,i}[\text{s}^{-1}]$ the heat and particle fluxes. These diffusion equations, obtained by flux-surface averaging of Ohm's law and moments of the Fokker-Planck equation [49], are then discretised using a finite element method by projecting the continuous functions $\{\psi(\hat{\rho}, t), T_{e,i}(\hat{\rho}, t), n_e(\hat{\rho}, t)\}$ on a base of n_{sp} cubic splines Λ_α [11]:

$$\begin{bmatrix} \psi(\hat{\rho}, t) \\ \mathbf{T}_{e,i}(\hat{\rho}, \mathbf{t}) \\ \mathbf{n}_e(\hat{\rho}, \mathbf{t}) \end{bmatrix} = \sum_{\alpha=1}^{n_{sp}} \Lambda_\alpha(\hat{\rho}) \mathbf{x}^\alpha(t), \quad \mathbf{x}^\alpha(t) = \begin{bmatrix} \hat{\psi}^\alpha(t) \\ \hat{\mathbf{T}}_{e,i}^\alpha(t) \\ \hat{\mathbf{n}}_e^\alpha(t) \end{bmatrix} \quad (2.1)$$

and defining $\mathbf{x}(t)$ as the state vector, so that the above transport equations can be rewritten in residual form:

$$\forall t, \quad \tilde{f}(\dot{\mathbf{x}}(t), \mathbf{x}(t), \mathbf{u}(t), \mathbf{p}) = 0, \quad \mathbf{u}(t) = \begin{bmatrix} I_p(t) \\ P_{aux}(t) \\ \vdots \end{bmatrix} \quad (2.2)$$

where \mathbf{u} and \mathbf{p} are the actuator and model parameter vectors and $P_{aux}(t)[\text{W}] = \int_V P_{e,i}(\hat{\rho}, t) dV$ is the input power integrated over the total plasma volume. For each time step k , a loop of Newton iterations is performed by computing the Jacobian matrices $\mathcal{J}_i^k = \frac{\partial \tilde{f}_k}{\partial x_i}$ until \mathbf{x}_k satisfies $\|\tilde{f}(\dot{\mathbf{x}}_k, \mathbf{x}_k, \mathbf{u}_k, \mathbf{p})\|_2 < \epsilon_{tol}$, i.e. the residual is below a given tolerance ϵ_{tol} , or until they reach the maximum number of iterations imposed for the simulation.

Particle sources are not yet included in the model, such that $S_e = 0$. Similarly, the heat flux $Q_{e,i}$, is assumed to be proportional to $n_{e,i} \chi_{e,i} \frac{\partial T_{e,i}}{\partial \hat{\rho}}$, after neglecting convective and pinch terms, including the particle flux $\Gamma_{e,i}$ contribution. The latter appears in the electron density diffusion equation as: $\Gamma_e \sim -D_e \frac{\partial n_e}{\partial \hat{\rho}} + V_e n_e$. The diffusivity coefficient $\chi_{e,i}$ and V_e/D_e are then to be evaluated through one of the fast transport models implemented in RAPTOR, namely the ad-hoc analytical formulation [50], Bohm-gyroBohm model [51], gradient-based model [19] (all based on empirical observations of the plasma confinement) and the QuaLiKiz neural network surrogate model [52]. These reduced models allow RAPTOR to bypass the numerically demanding calculation of tokamak nonlinear turbulence, thus making it particularly suitable for applications requiring rapid transport simulations.

In this work, we refer to a *pre-shot simulation*

as a rapid prediction of a plasma discharge trajectory, given a fixed equilibrium, derived from a set of programmed engineering parameters and validated only against past experiments, to help in the preparation, validation and optimization of a scenario. We call *pulse schedule* the set of engineering parameters and pre-computed information that is required by RAPTOR and FBT before the shot, currently including: requirements for the total plasma current in-vessel position and shape, engineering parameters of the heating systems (power, absorption factor, etc.) and gas reference. TCV is equipped with two NBI launchers and multiple gyrotrons. We focus in this work on ohmic and NBI-1 heated cases, since NBI is the primary heating system used for H-mode studies in TCV. The primary challenge of rapid full discharge simulations lies in the interdependence of transport equations and equilibrium, heating and current drive sources. We present here the choices that have been made in the spirit of keeping the model fast, flexible and easily expandable.

General assumptions.

- TCV plasmas are mainly composed of (D) deuterium main ion and (C) carbon impurities. Their concentration is determined using the quasi-neutrality equation:

$$\frac{n_D}{n_e} = \frac{Z_C - Z_{eff}}{Z_C - 1} \quad \text{and} \quad \frac{n_C}{n_e} = \frac{1}{Z_C} \frac{Z_{eff} - 1}{Z_C - 1}, \quad (2.3)$$

assuming a flat and constant profile of the effective charge $Z_{eff} = 1.5$.

- The NBI-1 deposition profiles are modeled by simple Gaussian profiles centered at radius $\hat{\rho}_{dep}$ and with a width w_{dep} over the normalized radius. The deposited power is then evaluated from the programmed injected power, by removing 15% of beam duct losses and applying a factor 55% to account for the total absorption into the thermal plasma, notably removing charge exchange losses [53]. Since NBI heating is predominantly central in TCV, it is modeled using a centered deposition profile of width 0.25 in $\hat{\rho}$ and zero current drive.

Transport and pedestal. The gradient-based model [19] is used to evaluate the heat and particle transport coefficients, $\chi_{e,i}$, $V_{e,i}$ and $D_{e,i}$. This model is based on the observation that radial transport usually behaves in a critical regime, in which the logarithmic gradients in the intermediate region between a sawtooth inversion $\hat{\rho}_{inv}$ and pedestal $\hat{\rho}_{ped}$ radii remain "stiff" [55–58]. This critical regime is found to emerge at a threshold value of logarithmic temperature gradient $\nabla T/T$, below which ITG and TEM become marginally stable. It is thus predominant in this central region, where the temperature increases towards the magnetic axis, while rarely

Mode	Shape	λ_{T_e}	λ_{T_i}	λ_{n_e}	$T_e _{sep}$ [eV]	$T_i _{sep}$ [eV]	$n_e _{sep}$ [10^{19}m^{-3}]	$H_e^{98(y,2)}$	$H^{98(y,2)}$
L	PT	3.2	3	2	20	16	0.5	0.4	0.7
H	PT	2.3	2.5	1	100	80	1	0.5	1
L	NT	3	3	3	20	16	0.5	0.5	1

Table 1: Typical parameters used in the gradient-based model depending on the confinement mode and triangularity (positive, PT, or negative, NT) including: the logarithmic gradients λ_σ and boundary conditions at the separatrix $T_\sigma|_{sep}$, and the electron $H_e^{98(y,2)}$ and total $H^{98(y,2)}$ confinement factors to the ITER H98(y,2) baseline scaling law [54] used as feedback reference for the PI controller.

observed in the colder edge region, whose gradient remains above the threshold [58, 59]. This observation allows to divide the electron and ion temperatures ($\sigma = T_{e,i}$) and electron density profiles ($\sigma = n_e$) in three separate regions:

$$-\frac{d \ln \sigma}{d \hat{\rho}} = \begin{cases} 0 & \text{for } 0 < \hat{\rho} < \hat{\rho}_{inv} \\ \lambda_\sigma & \text{for } \hat{\rho}_{inv} < \hat{\rho} < \hat{\rho}_{ped} \\ \frac{1}{\sigma} \mu_\sigma & \text{for } \hat{\rho}_{ped} < \hat{\rho} < 1, \end{cases} \quad (2.4)$$

where the linear peripheral gradient μ_σ is a non-stiff parameter of the model corresponding to the pedestal gradient. As noted in [58], L-modes also have a clear pedestal gradient, hence this model allows to unify L- and H-modes stationary profile representations. Full simulations of ASDEX-Upgrade [19, 21], TCV [19] and DEMO [22] discharges using the RAPTOR gradient-based model confirmed that the inverse scale-length for the electron temperature λ_{T_e} ($\sim a/L_{T_e}$) and density λ_{n_e} are indeed mostly constant across a stiff radial region, extending from $\hat{\rho}_{inv} \sim 0.2$ (depending on the $q = 1$ location) to $\hat{\rho}_{ped} \sim 0.8$ at TCV, and are essentially independent of plasma parameters such as the plasma current I_p , power sources $P_{e,i}$, line-averaged density n_{el} or triangularity δ (as shown in [58]); while the linear peripheral gradients μ_{T_e, T_i, n_e} exhibits a non-stiff behavior, typically responsible for variations in confinement during the discharge. In this model, the value of the non-stiff electron temperature gradient μ_{T_e} is modified by a PI controller to match a total confinement factor $H = \tau_E / \tau_E^{scal}$, scaling the energy confinement time obtained during the discharge, $\tau_E = W / P_{loss}$, with a data-driven scaling law τ_E^{scal} , with $P_{loss} = P_{oh} + P_{aux} - \frac{dW}{dt}$ the power loss. The total thermal energy $W = W_{tot} = W_e + W_i$ or electron energy $W = W_e$ is used in these computations, depending on the model chosen for the ion temperature, as detailed in the next paragraph. Similarly, μ_{n_e} is controlled to match the line-averaged density n_{el} . This model is thus able to follow any change in confinement and plasma density, if known beforehand, by modifying the height of the pedestals in a dynamic way. Boundary conditions at the separatrix $T_\sigma^{sep} = T_\sigma(\hat{\rho}) = 1$ are kept constant in each confinement phase of the discharge, following typical values observed experimentally. Their values and those of the logarithmic gradients λ_σ are reported in Table 1. Such simple model eliminates the need for complex pedestal physics, although it does require a starting hypothe-

sis about the confinement quality. In fact, choosing the gradient-based model for the pre-shot simulations was directly dictated by the need to solve the diffusion equations from the magnetic axis to the last closed flux surface, and the need to rely on a simple, robust transport model, which could match most of the TCV experimental data simulated in this work and easily cover L- and H-mode phases and transitions. In the present work, we compute the energy confinement time of reference τ_E^{scal} from the ITER H98(y,2) baseline scaling law [54].

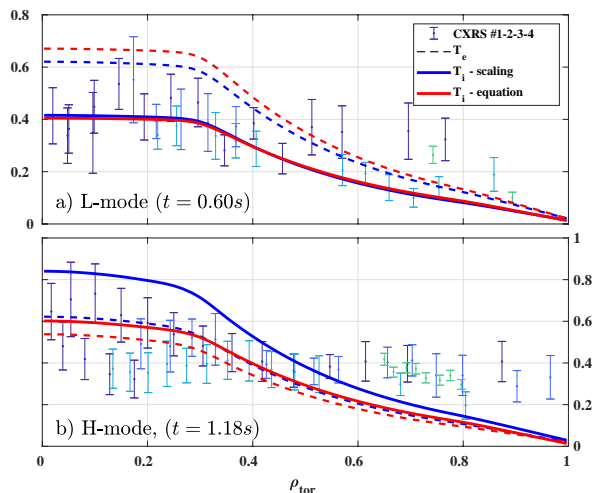


Figure 2: Comparison of two T_i estimations, using Eq. 2.5 with $H_e^{98(y,2)} = 0.5$ (in blue) and solving for the full ion heat equation with $H^{98(y,2)} = 1$ (in red), with the measurements of 4 CXRS systems for shot #81882, and comparison with T_e , in the L-mode ohmic phase (a) and in the NBI-heated H-mode phase (b). These models yield similar results, both predicting the CXRS measurements within their error-bars, except in the H-mode outer radii region, where measured values are biased by Edge Localized Modes.

Ion temperature. The total confinement factor $H^{98(y,2)} = \tau_E / \tau_E^{98(y,2)}$ is given as reference to the gradient-based model (see Table 1) when solving for the ion and electron heat equations together. Contributions from both species to the total transport are determined by the ratio of the ion to electron temperatures at the pedestal top, $\gamma = T_i / T_e|_{ped}$ and the logarithmic gradients $\lambda_{T_{i,e}}$, so that the edge

electron temperature gradient is controlled in relation to the total energy content W_{tot} . Values at the separatrix are set to $T_i|_{sep} = \gamma T_e|_{ped}$, such that the ion temperature gradient follows $\mu T_i = \gamma \mu T_e$. This fraction γ is then defined from the density and NBI power, such that the ion temperature at the pedestal doesn't exceed 90% of the electron temperature in ohmic plasmas and linearly decreases at lower densities, with the ad-hoc expression $\gamma = \min(0.4 + 0.5 n_{e,l} [5 \cdot 10^{19} m^{-3}], 0.9)$, to account for the weaker collisional coupling between ions and electrons at lower densities, while being set at 160% of the electron temperature when NBI heats up the ions. In these phases, NBI heats up both ion and electron species. 60% of the absorbed power is given to the ions in the simulations, while the total power absorbed by the thermal plasma (electrons and ions) is used in $\tau_E^{98(y,2)}$, reducing the need for a precise ion to electron heating ratio. This assumption can be improved in the future by using fast codes like RABBIT [60] once validated for TCV. In ohmic phases, on the other hand, electrons are primarily heated by the ohmic power and heat up the ions through equi-partition. Solving the ion and electron heat equations together makes it possible to translate the difference in stiff transport between the two species.

Alternatively, the ion temperature can be scaled from the electron temperature T_e , using the ratio:

$$T_i/T_e = 0.14 \frac{n_e}{n_i} Z_{eff}^{-0.5} [n_{el} [10^{19} m^{-3}]]^{0.8} q_{95}^{0.6}, \quad (2.5)$$

which original formula, commonly used in TCV experimental analysis, was obtained from simulations of ohmic and EC heated scenarios, with $n_i = n_D + n_C$ the total ion density and q_{95} the safety factor at 95% of the enclosed poloidal flux. The dependence of T_i/T_e on the NBI power is implicitly given through the line-averaged density term. In this model, the confinement factor used for controlling the electron pedestal gradient is set to: $H_e^{98(y,2)} = \left(\frac{W_e}{W_{tot}}\right) H^{98(y,2)}$, with W_e the electron thermal energy. This simple scaling reduces the number of equations to be solved and thus, the simulation time (by 10–15%) and the risk of numerical oscillation due to non-linear interactions between ion and electron temperatures, but does not take into account the differences in transport and heat sources between the two species. Both models tend to give reasonable profiles for most of the shots. As can be seen for example in Fig. 2, accuracy of TCV CXRS measurements does not always allow one model to be preferred over another. In particular, predicted temperature profiles are highly influenced by their value at the pedestal top and during ELMy H-mode phases, where CXRS measurements tend to be less accurate. However, statistical comparison over a large shot database, presented in Sec. 3, show that solving for the ion heat equation give more correct results than the scaling in Eq. 2.5, at

the cost of a greater sensitivity of the model gradients control and thus the need for a higher time resolution.

L-H transitions. Transition from low (L) to high (H) confinement mode is triggered during the simulation when the power going through the separatrix verifies:

$$P_{sep} = P_{loss} - P_{rad} = P_{oh} + P_{aux} - P_{rad} - \frac{dW}{dt} > P_{LH}, \quad (2.6)$$

provided that n_{el} is above a minimum threshold, of around $3 \cdot 10^{19} m^{-3}$ for TCV. As in many carbon devices, the core radiated power can be neglected [61] such that we can assume $P_{sep} = P_{loss}$. Since the $\frac{dW}{dt}$ term is highly sensitive to variations in the controlled μ gradients, yet remains very small over most of the discharge, it is for now neglected. Following the same strategy as in [20], the power threshold P_{LH} follows the 2008 Martin scaling law [26]:

$$P_{LH} = \frac{2}{A_i} 2.15 \cdot 10^6 [n_{el} [10^{20} m^{-3}]]^{0.782} B_0^{0.772} a^{0.975} R_0^{0.999} \quad (2.7)$$

This scaling was obtained from a multi-machine database of single null diverted configurations with ion grad B drift towards the X-point (Fwd B_t),

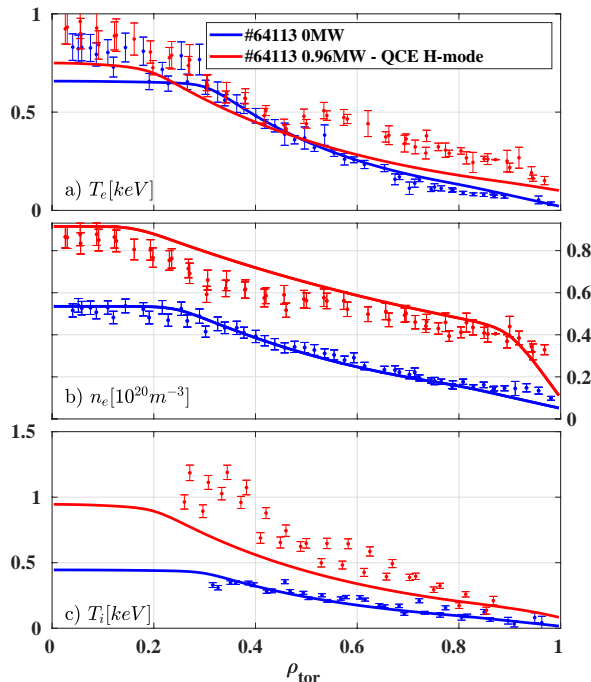


Figure 3: Evolution of (a) T_e , (b) n_e and (c) T_i profiles before and after the onset of NBI. As the H-mode is triggered and reaches a QCE regime, the TS measurements (markers with error-bars) show a slightly better confinement ($H_{exp}^{98(y,2)} > 1$) than the one modeled in RAPTOR (plain line), particularly shown in T_i . The experimental $n_{e,l}$ was used as input to this simulation.

$q_{95} > 2.5$ and neglecting cases with high radiation losses ($P_{rad}/P_{loss} < 50\%$). It notably excludes limited cases, where the H-mode access is rarely observed, but also double-null (DN) and SN configurations with unfavorable ion grad B drift (Rev B_t). Indeed, it has been shown [62, 63] that the H-mode access in SN diverted geometries strongly depends on the direction of the ion grad B drift, $\vec{v}_{D,i} = \frac{\mu}{2q_i B^2} \vec{B} \times \vec{\nabla} B$, and is systematically facilitated when the drift points *towards* the X-point location. On the other hand, the threshold for DN geometries remains uncertain. While an increase of P_{LH} has been reported in various machines [63–65], experiments on MAST-U [65], later reproduced on ASDEX Upgrade and NSTX [66], suggest that a lower threshold can be found in a true double-null configuration, i.e. provided that the two flux surfaces passing by the X-point are almost identical. This connected DN (CDN) can be characterized by a near-zero radial separation of the two X-point flux surfaces at the LFS mid-plane, $\delta r_{sep} < \delta r_{thr}$, with $2\delta r_{thr}$ being of the order of the ion thermal Larmor radius $\hat{\rho}_i$ or the SOL decay length λ_{SOL} , with SOL the scrape-off layer. This criterion can be continuously evaluated from one configuration to another, for both SN and DN configurations, choosing δr_{sep} equals to infinity or to the radial gap between the Last Closed Flux Surface (LCFS) and the wall when the secondary X-point is outside of the vacuum vessel (or limiter contour), and can be easily included in the prediction using the FBT fluxes and mapping. However, controlling precisely δr_{sep} is difficult to achieve experimentally, hence model predictions should be treated cautiously.

To include these various remarks, the power threshold P_{LH} is re-scaled with an ad-hoc factor α_{LH} , whose value is determined from the divertor geometry programmed in FBT, as:

$$\alpha_{LH} = \begin{cases} \alpha_l, & (\text{limited}) \\ f_{div}(s) = \alpha_f + (\alpha_u - \alpha_f)G(s), & (\text{diverted}) \end{cases} \quad (2.8)$$

where $s = \sigma_{fav} \left| \frac{\delta r_{sep}}{\delta r_{thr}} \right|$, $\sigma_{fav} = \pm 1$ is a factor which is positive in favorable configuration and negative in unfavorable configuration, $G(s) = \frac{1}{1+e^s}$. Thus, $f_{div}(s)$ is a continuous function of s , depicted in Fig. 11, that is characterized by two horizontal asymptotes, $\lim_{s \rightarrow +\infty} f_{div}(s) = \alpha_f = 1$ (favorable, Fwd B_t) and $\lim_{s \rightarrow -\infty} f_{div}(s) = \alpha_u = 2$ (unfavorable, Rev B_t), with $\lim_{s \rightarrow 0} f_{div}(s) = \frac{\alpha_f + \alpha_u}{2} = 1.5$ for a perfectly connected DN. In this work, α_l is set to a high prohibitive value, but could later be refined to include particular cases of H-mode access in limited configuration. In practice, most SN discharges that receive the power required to transition to H-mode have a clear favorable configuration such that s takes on large positive values. This is the case, for example, in the shot #64113 (Fig. 3), where the equilibrium configuration and NBI-1 power were programmed with the aim to obtain an H-mode in Quasi-Continuous Exhaust (QCE) regime [67]. If CDN configurations

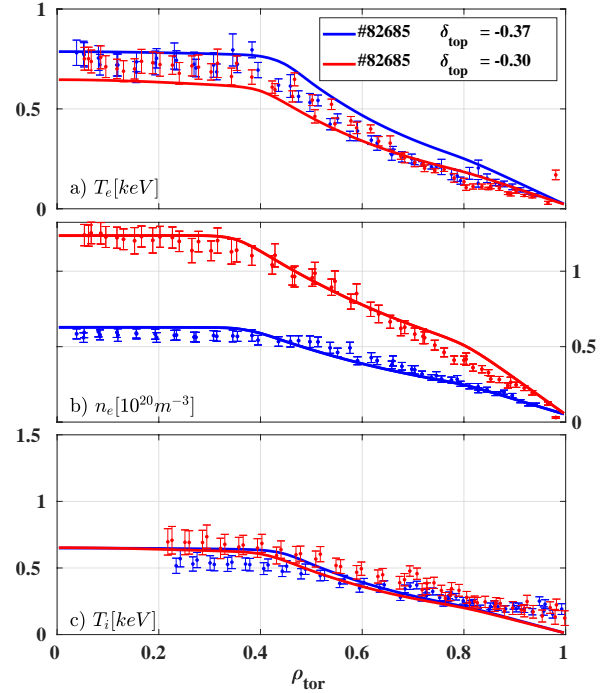


Figure 4: (a) T_e , (b) n_e and (c) T_i profiles of a negative triangularity (NT) shot. As the shaping decreases from $\delta = -0.37$ to -0.30 , the NBI-1 power is switched on and ramped up to $516 kW$, leading to an increase in density and total energy. With an $H^{98(y,2)} = 1$ and taking the experimental $n_{e,l}$, RAPTOR (plain line) matches the high confinement properties of the L-mode NT plasma, slightly over-estimating T_e in the ohmic (lower density) phase.

are later found to be favorable to L-H transitions, this strategy can be adapted by replacing f_{div} by a function of the form:

$$f_{div}^*(s) = G(-s)[\alpha_f - \eta e^{-\frac{s}{2}}] + G(s)[\alpha_u - (\alpha_u - \alpha_f + \eta)e^{-\frac{s}{2}}] \quad (2.9)$$

such that in perfectly connected DN, $\alpha_{LH} = f_{div}^*(0) = \alpha_f(1 - \eta)$ is lower than 1. It should be noted, however, that the quality of this prediction remains determined by our ability to control precisely the value of δr_{sep} during the discharge, the discrepancy between the equilibrium programmed in FBT and that obtained experimentally being outside the scope of this work.

Extension of the gradient-based model to negative triangularity plasmas. NT plasmas are less prone to transition to H-mode than standard PT plasmas [68, 69], while often achieving better L-mode performances. Recent results [41] showed that, in TCV, NT L-mode plasmas heated by NBI achieve a total pressure comparable to that observed in PT H-mode, while not switching to H-mode, even with a favorable X-point configuration, with sufficiently negative minimum triangularity [70]. In this work, values of α_{LH} listed in

Eq. 2.8 are increased by a prohibitive factor, such that H-mode access is inhibited in NT. Exact values can later be determined by modeling the access to the second ballooning stability, for example with CHEASE using the ballooning option [71] or coupled to the BALOO code [68, 72].

A new type of confinement state and associated peaking factors are added to the gradient-based model, which can now transition from positive to negative triangularity transport the same way as from L- to H- mode. In this work, plasma shape is considered NT when $\min(\delta_{up}, \delta_{bot}) < -0.2$, with δ_{up} and δ_{bot} the top and bottom triangularities. A smooth transition of 100ms is given to the controller to adapt the confinement properties, starting from the start of the NT shape, then ramping linearly from PT to NT parametrization. Fig. 4 shows an example of predictive simulation for a JET-like shaped NT plasma with an NBI power ramp, using NT parameters listed in Table 1. These parameters, selected to match the set of discharges simulated in this study (41 NT shots, among the 211 shots presented in Section 3), are kept the same and constant across the whole database simulated in this work. Shot #83575, whose KEP results are described in more details in Sec. 4.2, showed a confinement quality $H^{98(y,2)} > 1$, which could be inferred from previous experiments. It is interesting to note that we recover the same good core confinement of NT as in L-mode for λ_{Te} , while a better particle confinement, $\lambda_{ne} \simeq 3$, as in other NT experiments. The PT L- and H-mode values in Table 1 are also similar to those found in [46] for AUG, JET and TCV.

Line-averaged density. Governed by core-edge interactions, gas valve opening and auxiliary heating, the line-averaged electron density required for the gradient-based model can be complex to predict before the shot. While in many cases this can be reused from a previous experiment, it is also common for the density programming to be modified, making modeling a necessary step of the KEP. In TCV, the gas flow is, by default, feedback controlled on the FIR central chord measurements. In this case n_{el} can be modeled by a simple conversion from the FIR central chord reference to the line-averaged density. However, a strategy was required for phases in which feedback control is deactivated (feedforward only) or density is more difficult to control, such as NBI heated and H-mode phases. We therefore introduce a set of ad-hoc rules built on the shot programming, which are based on empirical observations of many discharges:

- If no heating power is expected and the feedforward gas input is zero, n_{el} undergoes an exponential decay with an ad-hoc lifetime of 125ms, reaching half its value, and is increased again if the plasma enters the limited regime
- if NBI-1 is on, n_{el} is increased by 30% to ac-

count for the neutral beam fueling and higher wall recycling.

The final ad-hoc trajectory is then increased by 30% when an H-mode is detected within the simulation, accounting for the better confinement and stronger wall recycling. These assumptions are TCV-related, but allow to predict a large variety of cases, from feedback to feedforward density control, and L- to H-modes, with simple conditions easy to test a posteriori. As discussed later, a proper generic density predictive model is needed to move forward, but is outside the scope of this paper.

Runtime optimization. The duration of a RAPTOR simulation is a decisive factor in making the KEP effective for tokamak operations. A simulation shorter than the latency between two discharges (typically between 5 and 15 minutes at TCV) allows to quickly validate and use the result of a new pulse schedule. Indeed, while the preparation of experiments can afford longer simulation times, the objective of the present KEP is to enable the rapid testing of various assumptions and to prepare the equilibrium of an experiment, without slowing down operations. Three factors mostly contribute to the computational time of the present KEP: the number of time steps used in RAPTOR, the evaluation of transport in the gradient-based model and the simultaneous resolution of the poloidal flux evolution and three kinetic profiles, T_e , n_e and T_i . Three strategies are used to reduce the computational time.

First, a fixed but non-equidistant time step is chosen using information from the pulse schedule, allowing for a higher time resolution in transients and a lower one in stationary phases. Transition times are defined by a criterion on the time derivative of the programmed plasma current \dot{I}_p , auxiliary power $\dot{P}_{e,i}$, elongation $\dot{\kappa}$ and triangularity $\dot{\delta}$. Keeping in mind that the model controller performs better if the time step is about an order of magnitude lower than the energy confinement time, τ_E , which ranges from milliseconds to tens of milliseconds in TCV, a minimum value $dt_{min} \leq 0.5\text{ms}$ is chosen for the sharp transitions, and a large dt_{max} up to 1ms is accepted elsewhere, with a smooth transition ensuring numerical continuity. This approach, driven by the knowledge of transient phases where shorter physical time scales are expected, enables to find a compromise between the simulation time and the model's ability to capture sudden changes in plasma dynamics. Second, a fixed scaling for the bulk n_i and carbon n_c ion densities is imposed, as shown in Eq. 2.3, avoiding extra quasi-neutrality matrix calculations. Finally, the Matlab solver body is generated and compiled in C, reducing the total simulation time by a factor of 2. With about 3 to 5 Newton iterations per time steps, the total

runtime, on a standard non-dedicated CPU², computed over simulations of 211 experiments (cf. Sec. 3) finally scales down to 2.3 ± 0.38 min per second of discharge, when solving for the ion heat equation, and 2.76 ± 0.68 min of simulation per second of discharge, when using the electron-to-ion scaling. This corresponds to 12.35 ± 7.36 s and 13.9 ± 4.64 s per average confinement time τ_E , while still leaving room for further optimization.

2.2 FBT

The MHD equilibrium of a toroidally confined plasma is a solution $\psi(R, Z)$ of the Grad-Shafranov equation [73, 74], which describes the force balance $\vec{\nabla}p = \vec{j} \times \vec{B}$ as a function of the pressure profile $p(\psi(R, Z))$ and flux function $F(\psi(R, Z)) = RB_\phi$ for an axisymmetric plasma. This solution is essential for solving any type of radial transport problem, as it determines the geometry at any radius. In RAPTOR, this must be provided externally by an equilibrium solver, whose choice depends on the nature of the problem. Among the available options, FBT [12] and LIUQE [27] from the MEQ suite are both categorized as *free boundary*, as they include in their computation the shape and location of the Last Closed Flux Surface (LCFS) as a function of the currents flowing through the external conductors. However, their scope differs: FBT is used before the shot to determine the coil currents required to maintain a certain shape (*inverse problem*), while LIUQE uses magnetic measurements to reconstruct the effective shape after or in real-time during the discharge (*reconstruction problem*).

Coil currents optimization. FBT is used in static mode: impacts of the plasma dynamics and passive vessel currents are neglected, such that the combination of active currents \mathbf{I}_a is estimated by minimizing the cost function:

$$\chi^2 = \underbrace{\sum_{\mu=1}^{N_C} w_\mu^C \delta\psi_\mu^2}_{\text{poloidal flux error}} + \underbrace{\sum_{j=1}^{N_a} w_j^P R_j I_j^2}_{\text{total resistive power}} + \underbrace{\sum_{j=1}^{N_a} w_j^T (I_j - I_{j-1})^2}_{\text{current diff. in adjacent coils}} + (\dots), \quad (2.10)$$

with (...) denoting a range of additional optimization terms, including extra constrains on the magnetic geometry. Following the notation in [29], we call \mathbf{I}_a and \mathbf{I}_y the sets of elementary currents flowing through the coils and plasma, respectively, on the computational grid X , such that $\mathbf{I}_y = \{j_{pl}(R_j, Z_j)\}$ with (R_j, Z_j) a point of the plasma domain (inside the LCFS) and j_{pl} the toroidal plasma current density. The poloidal flux error $\delta\psi_\mu^2$

is expressed as a distance of the solution ψ at a set of N_c control points (R_μ, Z_μ) to an optimization parameter F_b :

$$\delta\psi_\mu^2 = \|\psi(R_\mu, Z_\mu, \mathbf{I}_a, p', TT') - F_b\|^2. \quad (2.11)$$

The (R_μ, Z_μ) control points do not necessarily end up on the LCFS in the optimization result, but are most often chosen as such. It is common for example, when scheduling a diverted equilibrium, to impose the presence of a magnetic null in the vicinity of these points, where the primary X-point is expected, by adding extra constrains in χ^2 . The poloidal magnetic flux is computed from the Poisson like equation:

$$\Delta^* \psi = -2\pi R \mu_0 j_{pl} \quad (2.12)$$

$$= \begin{cases} -4\pi^2 (\mu_0 R^2 p'(\psi) + TT'(\psi)) & \text{in } \Omega_{pl} \\ 0 & \text{in } \Omega_{vac}, \end{cases} \quad (2.13)$$

where j_{pl} is the toroidal current density flowing through the plasma column, Ω_{pl} and Ω_{vac} are the plasma and vacuum domains respectively, and eq. 2.13 is the Grad-Shafranov equation (GSE), function of the internal plasma profiles $\{p' = \frac{dp}{d\psi}, TT' = \frac{1}{2} \frac{dT^2}{d\psi}\}$. Note that FBT uses the general MEQ convention for coordinates, COCOS=17 [75]. Finally, the value of the poloidal flux at the computational boundary $\delta\Omega_c$, results from a sum of contributions from the plasma and active coil currents:

$$\psi_b = \mathbb{M}_{by} \mathbf{I}_y + \mathbb{M}_{ba} \mathbf{I}_a \quad \text{on } \delta\Omega_c \quad (2.14)$$

which define the boundary conditions for eq. 2.12

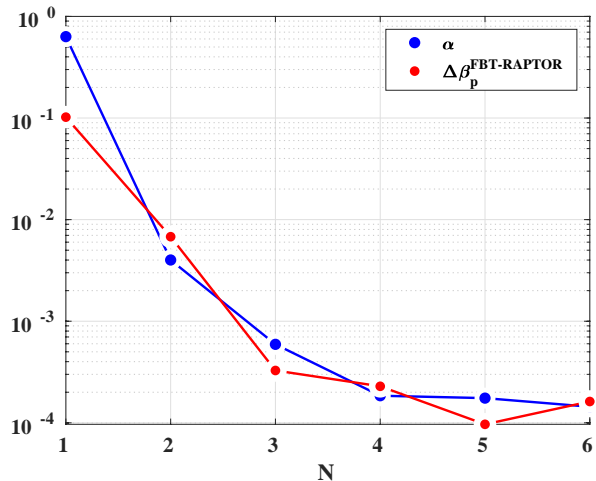


Figure 5: Result of the FBT-RAPTOR convergence for TCV shot #81882 after N iterations. $\alpha = p'_{\text{FBT}}/p'_{\text{RAPTOR}}$ and $\Delta\beta_{pol} = |\beta_{pol}^{\text{FBT}} - \beta_{pol}^{\text{RAPTOR}}|$. The y-axis shows the distance between these quantities and their final values at $N=7$.

2.3 FBT-RAPTOR coupling

With no prior estimation of the kinetic evolution and non-inductive current drive, the right-hand side of the GSE remains under-determined. In this case,

²Simulations were run in MATLAB R2017a (Parallel Computing Toolbox) using four concurrent workers on a shared compute server (2 × 8-core Intel Xeon E5-2660, 128 GB RAM; Fedora 22, x86_64). Reported runtimes are wall-clock times and may vary due to server load and MATLAB internal multithreading (up to 16 threads per worker)

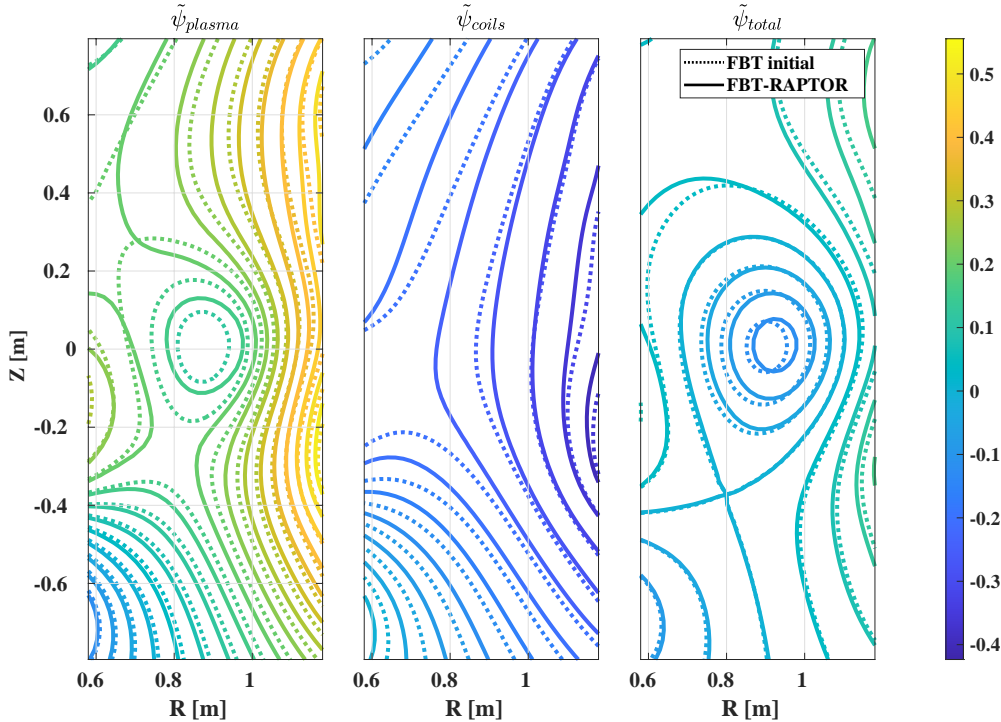


Figure 6: Plasma and coils contribution to the total poloidal flux in the H-mode phase ($t = 1.3\text{s}$) of #81882 centered around the total flux at the plasma boundary, $\tilde{\psi} = \psi - \psi_B$. Due to differences in poloidal beta, $\beta_{pol}^{\text{initial}} < \beta_{pol}^{\text{FBT-RAPTOR}}$, and internal inductance, $l_{i,3}^{\text{initial}} < l_{i,3}^{\text{FBT-RAPTOR}}$, the coupling (solid line) accounts for a stronger Shafranov shift $\Delta(\hat{\rho})$ than the initial FBT calculation (in dotted line)

the two free functions $p'(\psi)$ and $TT'(\psi)$ are usually built on simple basis functions which take, for the majority of TCV shots, the polynomial form³:

$$p'(\psi) = \frac{1}{2\pi} a_{g=1}^p (1 - \hat{\psi}), \quad (2.15)$$

$$TT'(\psi) = \frac{\mu_0}{2\pi} \sum_{g=1}^{N_T=2} a_g^T (1 - \hat{\psi})(-\hat{\psi})^{g-1}, \quad (2.16)$$

with $\hat{\psi}(R, Z) = (\psi(R, Z) - \psi_A)/(\psi_B - \psi_A)$ the normalised poloidal flux, ψ_A and ψ_B the values of the poloidal flux at the plasma axis and boundary; and it is standard practice for operators to parametrize their a_g coefficients (namely, to scale the plasma pressure and on-axis q) based on their experience of a given scenario. This method has remained in use for many years at TCV, thanks to the teams' expertise and to the relative robustness of the shape to differences in internal profiles. However:

1. its immediate success depends on operators experience, acquired through many years of practice
2. changes in parameters are sometimes driven by operational needs rather than by a realistic predictive estimate (e.g. it is common practice

to assume a flatter current distribution (higher q_A) in FBT, making sure the experimental inductance is higher or equal to the one assumed in FBT, with the aim of lowering elongation experimentally.)

3. transition times, e.g. from L to H mode, can be difficult to anticipate accurately without a model
4. and regardless of the quality of the programming, the simple formulation of $p'(\psi)$ and $TT'(\psi)$, typically (eq. 2.16) linear for the former and quadratic for the latter, cannot be a correct description of actual plasma profiles, especially in H-modes.

These approximations affect the plasma current in the Poisson like (Grad-Shavranov) equation (2.13) and its boundary condition (2.14), hence affecting the poloidal flux error and result of the PF coil currents optimization. First of all, the choice of β_{pol} and q_A (or l_i) determines the rate of change of the Shafranov shift $\Delta(\hat{\rho})$, i.e. the outward radial displacement of the magnetic surfaces with respect to the geometric (cylindrical) center of the plasma, with respect to the minor radius, $\Delta'(\hat{\rho})$. This shift comes with an increased compression of magnetic surfaces in the Low Field Side (LFS) of the plasma, responsible for a hoop force driving the plasma outward. If $\beta_{pol} + l_i/2$ is underestimated in the calculation, the vertical magnetic field virtually applied by the PF coils to compensate for

³General formulation of these standards basis functions accept any positive real values of powers of $\hat{\psi}$ (including non-integer values) and is therefore not strictly speaking polynomial.

this force [76] is underestimated, with the risk of the risk of introducing errors in the radial plasma position. Moreover, as stated in 2, the distribution of current in the plasma column influences the strength of the quadrupole term added to the vertical field to maintain the vertical plasma stability with a certain elongation [76]. Quantities impacting the growth rate of a vertical instability — for example, the plasma radial position, elongation and inner and outer gaps [77] — are therefore not immune to inaccuracies in p' and TT' profiles, whose consequences may range from a slight misalignment of the shape to a vertical displacement event (VDE). To address these limitations, we propose to constrain $p'(\psi)$ and $TT'(\psi)$ using the RAPTOR pre-shot model presented in Sec. 2.1. In this section and for the rest of the paper, we express the poloidal beta and internal inductance by their ITER design definition [78], used in both FBT and RAPTOR:

$$\beta_p = \frac{8}{3} \frac{W_{th}}{\mu_0 R_0 I_P^2} \equiv \frac{2}{3} \frac{W_{th}}{W_{pol}}, \quad l_{i,3} = \frac{2V \langle B_{pol}^2 \rangle_V}{\mu_0^2 I_P^2 R_0}. \quad (2.17)$$

where W_{th} is the total thermal energy, B_{pol} the poloidal magnetic field, $\langle B_{pol}^2 \rangle_V = \frac{1}{V} \int B_p^2 dV$ and V is the plasma volume.

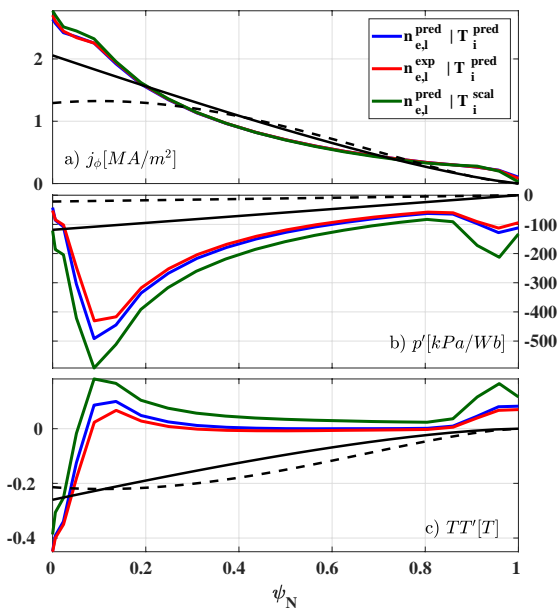


Figure 7: Comparison of RAPTOR j_Φ (a), p' (b) and TT' (c) profiles at $t = 2$ s using, for the line-averaged density, the pre-shot estimate (blue, green) shown in Fig. 16f, which is overestimated by about 20% at that time, or experimental post-shot values (red), and using the predicted T_i (blue, red) or the electron-to-ion scaling (green), Eq.2.5; in black are the simple polynomial FBT profiles used in reference shot #81882 (solid line) and in #83738 (dashed line, also used as initial conditions for the KEP).

The new FBT basis functions are chosen to keep one degree of freedom from the RAPTOR profiles: a small $\Delta\alpha = |\alpha - 1|$ correction is applied

to p' to follow the plasma current target I_p , while strictly keeping TT' from the simulation. The previous solution for the plasma current distribution, \mathbf{I}_y , is used as an initial guess to the new FBT run to facilitate convergence. If a solution is not reached after 20 iterations, the plasma domain $\partial\Omega_{pl}$ is frozen, while the iteration continues until convergence. This approach has proven effective, as non-convergence typically results from small oscillations between two points on the computational grid, and allows a solution to be found for nearly all the equilibria, while keeping the standard mesh used in TCV, $n_R \times n_Z = 28 \times 65$. When an iteration of the coupling does not converge at a given time, the previous converged solution for that time is taken. Thus, in the few cases where an equilibrium fails to converge from the first KEP iteration, the initial FBT equilibrium, with standard basis functions, is retained. The last converged solution is then linearly interpolated across the full RAPTOR time grid, and passed in a matrix form to the next RAPTOR simulation. The gradients at the pedestal, μ_{ne} and μ_{Te} , can also be passed from the previous RAPTOR simulation to the next as a feedforward trace to ease the work of the gradient-based controller. Consistency between transport and equilibrium is obtained when p' and TT' take identical profiles in RAPTOR and FBT, corresponding to a basis function coefficient $\alpha = 1$. After iterating over the two codes sequentially, a systematic error on poloidal beta $\Delta\beta_{pol}^{\text{FBT-RAPTOR}}$ and $\Delta\alpha$ of less than 5% remains, due to residual differences in volume and radial resolution. By subtracting $\Delta\beta_{pol}^{\text{FBT-RAPTOR}}$ and coefficient α by their final error, Fig. 5 shows that the coupling successfully converges to its final solution within a few iterations, as shown in the example of TCV shot #81882, where a remaining difference of less than 1% to the converged values was obtained after only 2 steps. This rapid convergence can be explained by the quasi-unilateral nature of this coupling, as radial transport is only weakly sensitive to changes in geometry, and by the mutual independence of the static equilibrium solutions.

The choice of constraining $p'(\psi)$ or $TT'(\psi)$ to match I_p ensures that the shot's initial programming remains unaltered, despite small numerical discrepancies. Contours of the new poloidal flux, represented in Fig. 6, show a typical correction made to the total flux, $\psi_{total} = \psi$, plasma contribution, $\psi_{plasma} = \mathbb{M}_{xy} \mathbf{I}_y$, and coil contribution, $\psi_{coils} = \mathbb{M}_{xa} \mathbf{I}_a$, with the new radial profiles. Fluxes are centered around the total flux at the plasma boundary, $\tilde{\psi} = \psi - \psi_B$, whose exact value are linked to the radial derivative of the Shafranov shift at the boundary $\Delta'_B \sim \beta_{pol} + l_{i3}/2$ (Eq. 4.21 in [79]). The initial FBT programming is given a very low poloidal beta $\beta_{pol} = 0.07$ and high q on-axis $q_A = 2$, then used as initial condition to the coupling in order to better demonstrate the full pro-

cedure. After convergence, FBT-RAPTOR results in a stronger Shafranov shift, with $\beta_{pol} + l_{i,3}/2$ being multiplied by 2.2, and in the PF coils generating a stronger vertical magnetic field in the mid-plane. Keeping the same value of plasma current I_p , the new β_{pol} coming from RAPTOR and the q_A value corresponding to the new $l_{i,3}$ can also be directly imposed as constraints with the usual basis functions, resulting in the same $\beta_{pol} + l_{i,3}/2$ as in the coupling. Interestingly, the comparison (Fig. A.1) reveals that the Shafranov shift is not sufficient to explain the change in coil contribution, as the shape of the internal profiles is also responsible for a change in the flux induced by the plasma current, which causes a correction in the order of tens of Amperes in PF coil currents. In both cases, the vacuum vertical field is increased by 10–20mT around the midplane due to the higher Shafranov shift, thereby leading to a significant decrease and increase of the E_{4-5} and F_{4-5} coil currents respectively.

Fig. 7 shows an example of j_ϕ , p' and TT' profiles obtained with RAPTOR for different modeling assumptions, with comparison to the simple polynomial profiles initially programmed in FBT. We find that the choice of model for the ion temperature and the quality of the density estimate have a reasonably low impact on the p' and TT' used in Grad-Shafranov for that shot, compared to the profiles used initially.

The new I_a currents calculated by FBT are then included in the usual shot preparation. The ohmic transformer coil current needed to drive the target I_p trajectory and the eddy currents induced by the time variation of ohmic, PF and plasma currents, are computed at the stage from the FBT equilibria. Final values of the feedforward PF coil trajectories are then computed by adding corrections to the pre-computed FBT traces, so as to cancel the stray fields resulting from the transformer and eddy currents. Feedback control during the experiment further adds to the currents modification. The TCV hybrid control system is based on a set of switching matrices responsible for the allocation of coils to the various real-time control tasks, in particular the control of the PF coil currents, vertical and radial displacement, total plasma current and stray field coming from the ohmic (OH) circuit [80]. Two (external) PF coil combinations are typically selected for the vertical and radial plasma position control, while the internal G coil is used for vertical stability. Overall, the stray field correction of the feedforward traces and real-time feedback control both introduce a systematic gap between the coil currents prepared in the FBT run and the actual currents used during the experiment, which must be taken into account in understanding the results. The latter is discussed in Sec. 4.

3 Benchmark of the pre-shot prediction of 207 shots

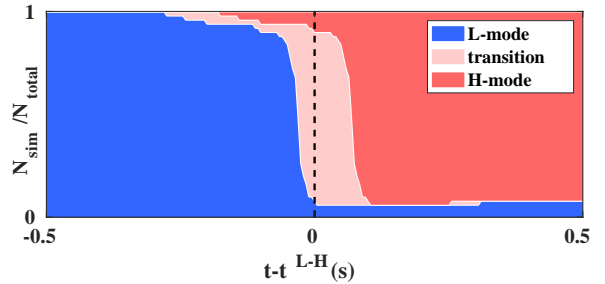


Figure 8: L–H transitions predicted by RAPTOR from the pulse schedule and experimental line-averaged density using Eq. 2.6 for 51 SN discharges for which a transition was detected from experiments by a confinement state classifier. Each simulation is time-aligned to the detection of either H-mode or D-mode (Dithering) by the classifier at t^{L-H} . The vertical axis represents the number of simulations N_{sim} predicted in each confinement state divided by the total number of simulations N_{tot} for a given time slice.

The methodology presented in Sec.2.1 provides a fast and automatic simulator of the kinetic profiles in the core plasma for full NBI-heated and ohmic discharges. By providing a pre-shot estimate of the internal profiles necessary for solving the Grad-Shafranov equation, Sec.2.3 showed that these results can be coupled to the FBT inverse equilibrium problem, forming what we refer to as a Kinetic Equilibrium Prediction. In this section, we present the application of this KEP to a wide set of TCV discharges, including 211 shots in the range 82000–83000, selected for their duration, availability of Thomson Scattering (TS) data, and excluding discharges with ECRH heating. This shot-base contains a variety of L- and H- mode plasmas in limited and diverted configuration, including NT discharges, and is therefore appropriate for testing the ability of RAPTOR to predict the H-mode phases with the extended Martin scaling law. All the simulations shown in this Section were performed providing the post-shot $n_{e,l}$ from experiments together with the pulse schedule as the accuracy of the $n_{e,l}$ ad-hoc model exposed in Sec. 2.1 and later used in the experimental validation in Sec. 4 does not yet allow for validation over a large shot database. To compare with our predictions, the actual time of transition from an L- to a Dithering (D-) or H-mode, denoted t^{LH} , is determined by a confinement state classifier [81] from diagnostic measurements available for each shot, integrated using DEFUSE [82].

Fig. 8 shows the results of the RAPTOR prediction for 51 of the 183 PT shots having an H-mode detected by the classifier at $t = t^{L-H}$, excluding the DN shot #82274, which is discussed below. For 48 of these shots, RAPTOR predicts a transition around t^{L-H} within a 100ms time-window.

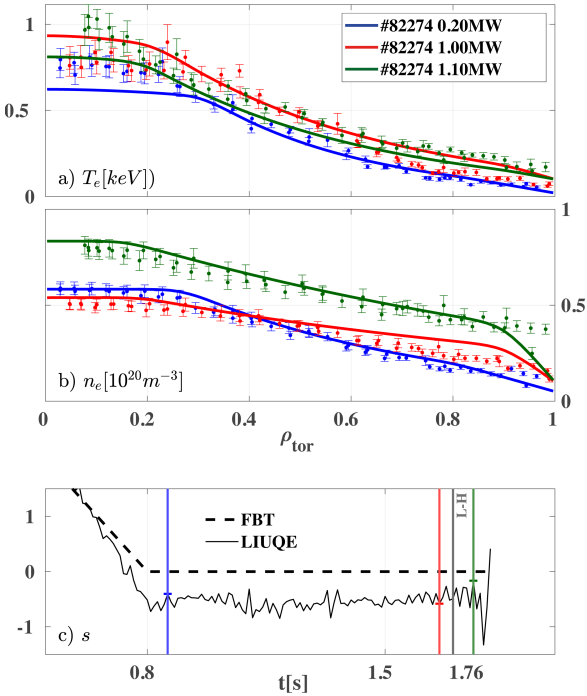


Figure 9: Evolution of T_e and n_e profiles during the NBI-1 power ramp of (DN) shot #82274. A delay occurs between the appearance of the H-mode pedestal (a, b) in TS measurements (markers with error-bars) and RAPTOR predicted profiles (solid line). (c) shows the evolution of $s = \sigma_{fav} \left| \frac{\delta r_{sep}}{\delta r_{thr}} \right|$. This value is programmed to 0 in FBT (dashed line), to target a DN, LIUQE post-shot (solid line) shows a slightly unfavorable configuration, delaying the access to H-mode. The NBI power ramps linearly from 168kW at $t = 0.8$ s to 1.12MW at $t = 1.8$ s. The experiment only transitions at $t = 1.7$ s (solid vertical grey line). The experimental $n_{e,l}$ was used as input to this simulation.

In the remaining 3 ohmic shots (continuous blue area, Fig. 8), the presence of an H-mode is detected with a low level of confidence and, in fact, no clear trace of ELM can be seen from the Photodiode (PD) signal of the H_α/D_α line emission, nor any H-mode pedestal in the Thomson Scattering profiles, indicating that the prediction made in RAPTOR, that these shots remain in L-mode, is correct. This good agreement can be explained by a clear restriction of the H-mode access to plasmas with favorable P_{sep}/P_{LH} and s values, as can be seen in Fig. 11. This figure shows experimental values for all of the 183 PT discharges simulated with the KEP, together with the f_{div} curves presented in Eqs. 2.8 (solid, used in the simulations) and 2.9. Each non-limited phase of a discharge is represented every 20ms, with a color corresponding to its confinement state, either detected by the classifier or manually corrected for the 3 ohmic shots mentioned earlier. While most L-mode plasmas have their P_{sep} below $f_{div}(s)P_{LH}$, some isolated blue points in the upper region can be seen from discharges be-

fore or after their transition to H-mode. Denser blue regions can also be seen in the vicinity of the f_{div} curve. These correspond to shots which are marginal and “resisted” the H-mode transition for a long period of time despite their favorable P_{sep} and s values. RAPTOR predicted an H-mode in at least one time sample in 25 of these discharges, including 21 ohmic shots that stayed in L-mode all along most probably due to the high X-point height of their configuration. This detrimental effect of the X-point height on the H-mode access has been demonstrated experimentally in [83, 84] and could be later added to the extended Martin scaling presented in Sec. 2.1. Among the 4 remaining NBI-heated discharges for which RAPTOR anticipated an H-mode transition that did not or took longer to appear, 3 come from a study of H-mode access in DN configurations: #82272, #82274 and #82275; with the NBI-1 power ramping from 180kW to 1.14MW in 1s. These 3 shots are interesting because they were programmed as perfectly CDN in FBT, i.e. with $s = 0$, such that the threshold is in between the favorable and unfavorable region, that is in between the dashed and solid black lines in Fig. 11. The 3 discharges behaved very similarly, with a late transition during the NBI-1 ramp and one shot #82274 is highlighted in Fig. 11. First the discharge ended up as an USN with s slightly below 0 ($\simeq -0.5$) as shown in Fig. 9c. Since f_{div} is varying rapidly in this region, having a slightly LSN, favorable $s \simeq +0.5$, would have led to a factor 1.25 instead of 1.75. We also show in Fig. 9 the profiles early in the power ramp and just before and after the transition. RAPTOR predicted a too early transition, as discussed here, and therefore a slightly lower l_{i3} . However the predictions with FBT-RAPTOR depend on the accuracy of the shape control in such cases. On the other hand, these shots are the only one to occupy the space between the dashed and solid lines. Since they all transit to H-mode late in the ramp, it shows that TCv does not exhibit a clear favorable effect of DN on the H-mode transition. However more shots are needed to characterize this region more systematically, including cases with varying radiated power.

Finally, an USN NBI-heated discharge in unfavorable configuration and close to the wall, #82547, is located above the f_{div} curve in Fig. 11, where RAPTOR predicts an H-mode, and below, when accounting for the core radiations from bolometer measurements (A.2). This shot did not transition to H-mode experimentally, suggesting that further refinement of the model by including impurity transport and line impurity radiation would also help in extending our H-mode prediction capability.

Comparison of the total energies obtained in experiments and simulations, with and without experimental $n_{e,l}$, and solving for the ion heat equation, are presented in Figs. 10 and A.3. Results obtained

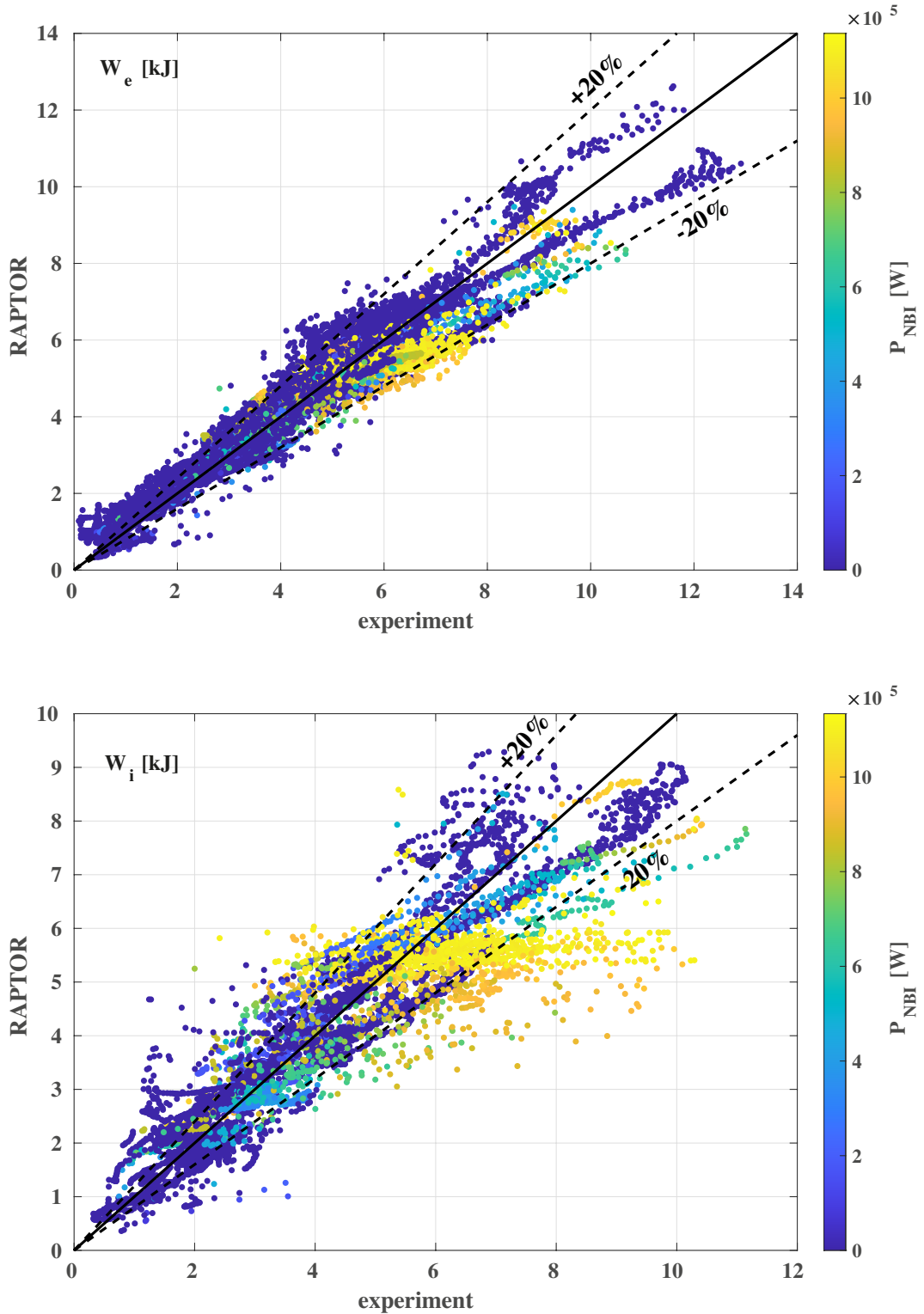


Figure 10: Comparison of the electron and ion energies predicted by RAPTOR with values reconstructed from experiments for, respectively, 211 shots with TS and 148 shots with CXRS measurements, at every measurement time instants. The dashed lines correspond to $W_{e,i}^{\text{experiment}} \pm 20\%$. RAPTOR predictions were made from the pulse schedule, using the line-averaged density from experiments and solving for T_i . The experimental value of W_i is more uncertain at high power with H-mode and ELM perturbations.

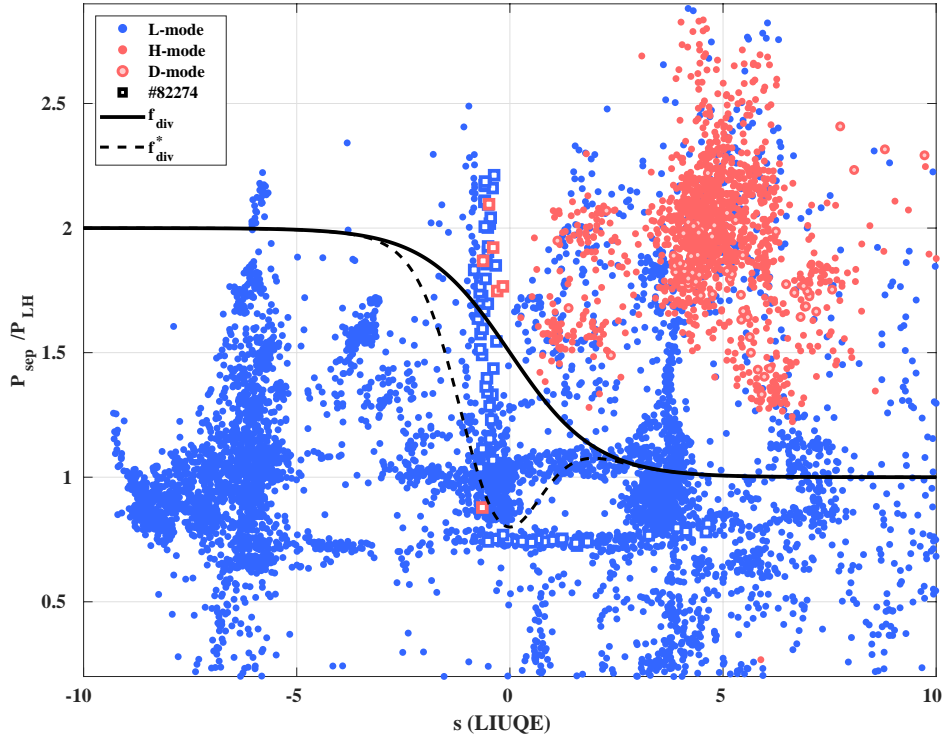


Figure 11: Illustration in black of the f_{div} (solid) and f_{div}^* (dashed), functions of $s = \sigma_{fav} \left| \frac{\delta r_{sep}}{\delta r_{thr}} \right|$, Eqs. 2.8–2.9. Each point corresponds to a time sample from 175 experiments having a diverted configuration, showing the dependence of the confinement state on the P_{sep}/P_{LH} ratio (computed from experimental data with the standard TCV analysis routines) and the s value (reconstructed with LIUQE); P_{LH} , from the Martin scaling with an additional weight at low line-averaged densities ($< 3e19m^{-3}$), and P_{sep} estimated assuming a fixed ratio of absorbed NBI power and no core radiation, in accordance with the assumptions made in the RAPTOR simulations. Shot #82274, a programmed double-null configuration, is highlighted in white squares and further described in Fig. 9. The outline of these squares is colored in the same way as the other points, showing the transition to H mode at the end of the NBI ramp, when the P_{sep}/P_{LH} is higher. An alternative version of this plot, accounting for the core radiation in P_{sep} , is shown in appendix (Fig. A.2). The L, D and H (see legend) phases are marked according to the plasma state classifier [81].

with the electron-to-ion scaling, only solving for the electron temperature and density using the electron confinement factor $H_e^{98(y,2)}$ and $n_{e,l}$, are shown in Fig. A.4. As shown by the three scans, W_e is predicted within 20% for essentially all cases, as well as W_i for most cases when T_i is predicted by RAPTOR. The uncertainties are larger for the ion energy content than for the electron energy. The W_i measured by CXRS has larger error bars than TS, particularly in H-mode, as Edge Localised Modes tend to create fluctuations in the passive signal and bias the estimations. Hence RAPTOR is overall clearly predicting within the error bars the full time evolution of the discharges, from ramp-up to ramp-down. The $n_{e,l}$ uncertainty affects the prediction of both electron and ion energies (Fig. 10 vs. Fig. A.3), although its impact is more pronounced on specific shots. All three results, solving the four equations taking $n_{e,l}$ from experiment (Fig. 10), solving three equations with $n_{e,l}$ from experiment and electron-to-ion scaling (Fig. A.4), and the fully predictive model with four equations and predicting $n_{e,l}$ from the pulse schedule (Fig. A.3), give similar predictions for the L- to H-mode transitions.

Following the convergence study presented in Sec. 2.3, three iterations between RAPTOR and FBT were performed for each of the simulations presented above, starting from the initial FBT equilibrium. On average, 6.0 ± 1.5 minutes of cumulated RAPTOR and FBT simulations were necessary for each iteration of the KEP (18 ± 4 minutes per total coupling). We show in Fig. 12 a distribution of resulting coil currents for times of interest, i.e. for equilibria with plasma currents exceeding 20% of the flat-top value. Since the PF coil currents can take positive or negative values, e.g. depending on the plasma shape or the sign of the plasma current, the difference is calculated from the absolute value, such that positive and negative values of $\Delta|\mathbf{I}_a|$ correspond to an increase or decrease in amplitude respectively. This distribution reveals that the correction made by the KEP occasionally reaches several hundreds of amperes, but is more commonly measured in tens of amperes, depending on the correctness of the initial β_{pol} and q_A and the phase in the discharge. Most equilibria are programmed at the beginning and end of a shot, during the I_p ramps : each discharge is prepared with an average of 3.2 ± 7 FBT equilibria for total pulse durations of 2.04 ± 0.24 s, over which 9.6 ± 0.9 (30%) and 10.3 ± 3.2 (32%) belongs to the first and last 200ms. Usually, the KEP provides greater corrections in the middle of the shots, where changes in thermal energy can be more important, but the equilibrium remains more steady. It is thus of interest, when preparing for an experiment, to increase the resolution of the FBT-RAPTOR coupling by adding more equilibria in this phase, similarly to what is done in the preparation of experiments presented in Sec. 4. As RAPTOR is only run for times

with $I_p > 50$ kA, an average of 3.0 ± 0.8 equilibria is not coupled at the beginning of the shots. Simulations converge up to 0.08 ± 0.09 s in average before the end of their I_p trace, corresponding to 4.3 ± 7.2 missed RAPTOR input profiles in coupling with equilibrium. 100% of FBT equilibria converged up to the last iteration given a converged RAPTOR input profile. The KEP robustness remains therefore mainly limited to the convergence of the latter. All equilibria for which the KEP did not converge from the first iteration (i.e. equilibria for which a converged RAPTOR input profile was missing) are kept with the standard basis functions.

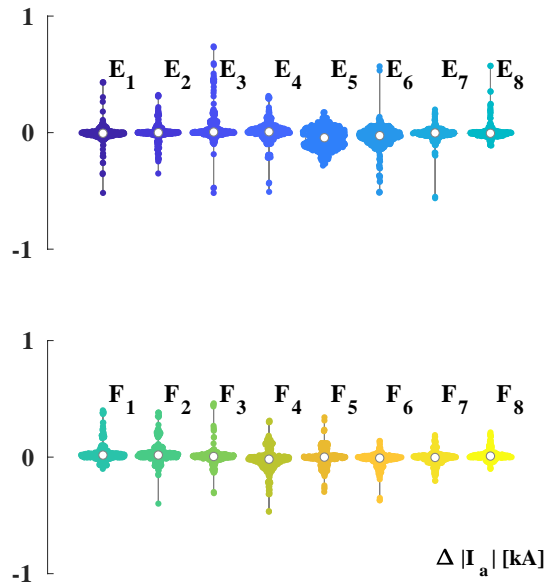


Figure 12: Distribution of differences in feedforward PF coil currents (in absolute value) computed by FBT-RAPTOR for various TCVC shots, $\Delta|\mathbf{I}_a| = |\mathbf{I}_a^{\text{KEP}}| - |\mathbf{I}_a^0|$. Equilibria in early ramp-up and late ramp-down phases, less sensitive to the coupling, are excluded from the distribution by selecting times for which $I_p > 20\% I_p^{\text{max}}$. PF coils are colored as in Fig. 1. A cluster of points around $\Delta|\mathbf{I}_a| = 0$ indicates that a large number of these corrections remain relatively small (around ten amperes), while larger corrections, on the order of hundreds of amperes, define the upper bound.

4 Experimental validation

4.1 Standard H-mode scenario in LSN configuration

This section presents in more detail the pre-shot simulation and FBT preparation of TCVC shot #81882. This shot is a standard scenario with an injection of 1MW of NBI power in the flat-top phase and a mainly inductive current profile. Starting from a short 100ms ramp-up in limited configuration, the plasma becomes diverted at $t = 0.4$ s forming a lower X-point, with ion grad-B drift pointing downwards, in the favorable direction. Shortly after the NBI injection, the power threshold is reached,

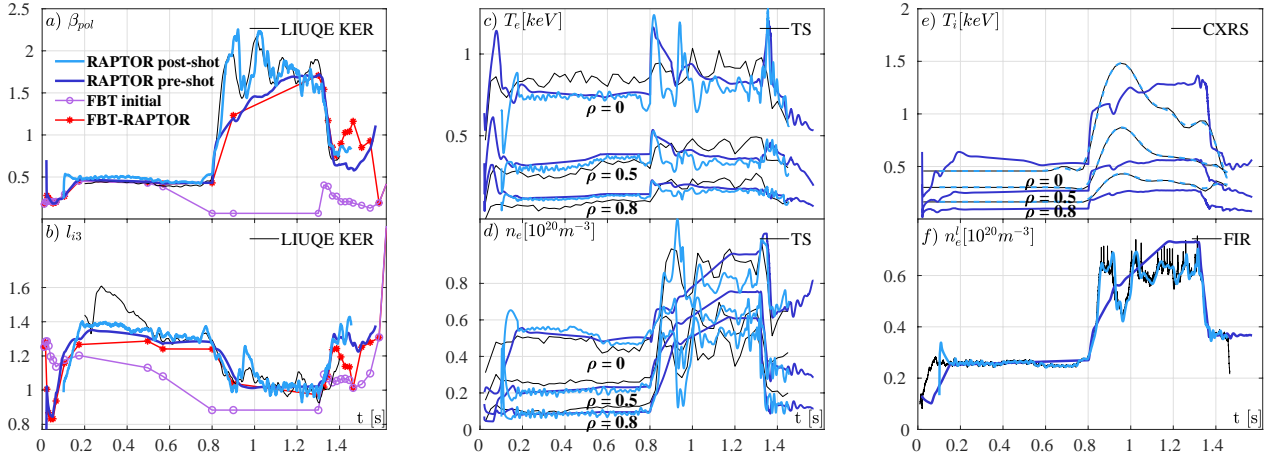


Figure 13: Overview of the KEP performed for TCV shot #81882. The pre-shot simulation (fully predictive without density measurements, dark blue) is compared to a post-shot simulation (light blue) using the same peaking and confinement factors but taking the line-averaged density and T_i from experiment. TS, CXRS and FIR data of shot #81882 are displayed in black in (c-f) as well as LIUQE-KER in (a-b). The coupling used an initial FBT run with a low β_{pol} and $l_{i,3}$ (in purple, (a-b)) used for the preparation of shot #83738 and the result after 2 iterations (in red) was used to prepare #83740, both shown in Fig. 14

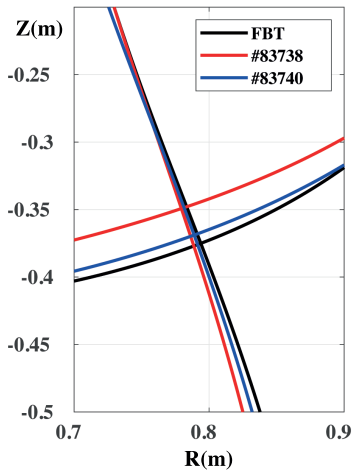


Figure 14: FBT X-point target and LIUQE shape reconstructions obtained in the H-mode phase for shot #83738, prepared with an initial FBT equilibrium with low- β_{pol} and low- $l_{i,3}$, and shot #83740, prepared with the FBT-RAPTOR correction

triggering the transition to H-mode at $t = 0.8$ s. The electron confinement quality H_e^{98} is thus slowly increased from 0.4 to 0.5, while the target n_{el} is increased up to $n_{el} \simeq 7 \cdot 10^{19} \text{ m}^{-3}$, as shown in Fig. 13. In this case we used the T_e/T_i scaling law to predict T_i . The logarithmic gradient for the electron temperature λ_{Te} and the density λ_{ne} decrease following Table 1, flattening the profiles with the rise of the pedestal and the change of the plasma parameters, modifying the turbulent regime [85, 86]. Comparison with the post-shot simulation (light blue, Fig. 13), shows that the variations in $n_{e,l}$ and ion temperature are responsible for the small difference in β observed in Fig. 13a.

The KEP is initialized from a standard FBT

programming with polynomial basis functions, low β_p and high q_A (purple line in Fig. 13) keeping the shape, position and plasma current desired for the shot. Starting from a deliberately degraded estimate of β_p and q_A ($l_{i,3}$) allows us to test the robustness of the method and its capability to correct any kind of initial condition. Indeed, consistent values of the internal inductance $l_{i,3}$ and poloidal beta β_{pol} are obtained between FBT and RAPTOR from this equilibrium after only 2 iterations, changing the flux distribution and the estimated combination of poloidal field coil currents I_a required for maintaining the shape. These new feedforward traces show significant differences during the H-mode phase, reaching several hundred amperes where the change in β_{pol} and $l_{i,3}$ is more significant. Variations in flux distribution are particularly pronounced in regions of low poloidal field, such as the primary X-point target, even during the least affected phases of the discharge. In these regions, the PF coil flux distribution is influenced as much by differences in β_{pol} and $l_{i,3}$ as by the shape of p' and TT' , though sometimes with a reduced impact on coil currents. We tested the pulse schedule experimentally, with the initial FBT programming (#83738) and with the new FBT-RAPTOR result (#83940), as described above. While both shots stayed generally stable with a good plasma shape, a better alignment of the X-point with the FBT target was observed all along the discharge prepared with FBT-RAPTOR, as shown in Fig. 14 and confirmed with the MANTIS [87] inversion.

Comparison between LIUQE MER and KER is important for validating the KEP predictions, in particular for the evaluation of the internal induc-

tance l_{i3} . As mentioned notably in [88], configurations with identical values of $\beta_{pol} + l_{i3}/2$, sharing the same plasma boundary and plasma induced magnetic field on the same boundary, can be attributed to various equilibria with different pressure and current density profiles. In the standard LIUQE Magnetic Equilibrium Reconstruction (MER), which only relies on magnetic measurements to reconstruct the equilibrium of an experiment, the diamagnetic loop (DML) helps distinguishing the TT' from the p' term in the Grad-Shafranov equation [27], providing an estimate of l_{i3} over β_{pol} . Fig. 15 shows that the ratio using the DML for shot #81882 differs significantly from the one obtained when performing an interpretative LIUQE-ASTRA KER [29] using the kinetic profiles coming from Thomson Scattering and CXRS data, and the current diffusion computed within ASTRA. While the DML constrained MER predicts an increase of internal inductance when passing from L to H-mode (as can be seen by comparing results with and without the DML constraint), the opposite behavior is observed in the interpretative KER, similarly to what is obtained in the pre-shot RAPTOR simulation (Fig. 13), which is coherent with the emergence of an additional bootstrap current density at the H-mode pedestal. Although the true value of the inductance may lie somewhere between the two results, the idea that the internal inductance decreases with the appearance of this edge bootstrap current term is more realistic. This example illustrates how kinetic-equilibrium couplings, e.g. the RAPTOR-FBT KEP before the shot and a fortiori the ASTRA- or RAPTOR- LIUQE KER after (or during) the shot, can provide additional information beyond results from magnetic measurements alone, by providing a physics-based estimate of l_{i3} and β_{pol} .

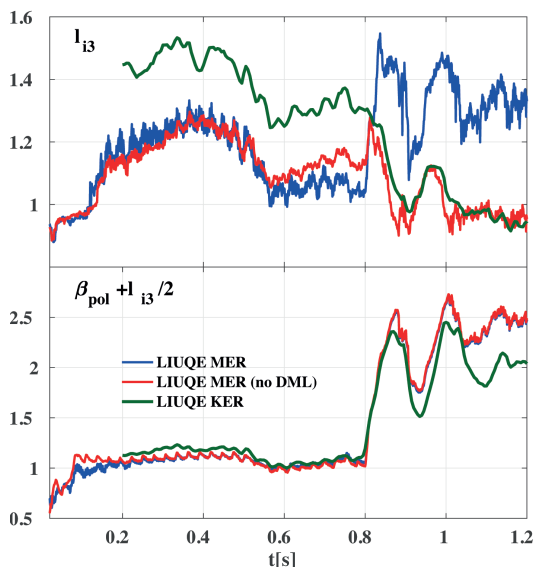


Figure 15: Comparison of l_{i3} and β_{pol} reconstructed from LIUQE KER and LIUQE MER with and without the DML measurement.

4.2 Negative-triangularity L-mode scenario with SF divertor target

Fig. 16 shows the pre-shot simulation of shot #83575, an upper negative triangularity (NT) L-mode plasma with up to 460kW of NBI-1 power. The plasma starts in PT-LSN configuration during the current ramp-up and overshoot, then transitions to an upper NT with snowflake divertor (SF) shape at $t = 0.7s$ [89] (see Fig. 1 for the SF shape). An electron confinement

$H_e^{98(y,2)} = 0.6$ is used for predicting the NT phase of the discharge, based on previous discharges, with peaking factors as in Table 1. This yields a total $H^{98(y,2)} \sim 1.2 - 1.3$ using T_i from Eq. 2.5. The line-averaged density is predicted from the pulse schedule, keeping the assumptions made for PT L-mode plasmas. Fig. 16 shows the resulting pre-shot simulation (dark blue) used for the coupling (in red), compared with the experimental results. The confinement of the discharge outperformed the prediction: the standard TCV post-shot analysis estimates the total confinement factor $H^{98(y,2)}$ between 1.3 and 1.5 in the NT-phase, mainly resulting from higher ion temperatures than predicted by the scaling (Fig. 16e). A post-shot simulation, repeated (in sky blue) with the same electron confinement parameter ($H_e^{98} = 0.6$) and input NBI power, but taking the line-averaged density and ion temperature from experiment, yield a total confinement factor between 1.5 and 1.6, resulting from a more conservative absorbed fraction of the NBI power in the simulations. Following the same procedure as in 4.1, we repeated the scenario experimentally, with the initial FBT programming (purple, Fig. 16) for shots #[83946, 83947, 83950] and with the new FBT-RAPTOR results (red) for shots #[83926, 83978], providing the new feedforward set of PF coil currents to the shape controller. Negative triangularity plasmas are known to be more difficult to control vertically [77, 90], as confirmed by FGE [29], which computes a vertical growth rate of 1389Hz, compared to 115.97Hz for shot #81882. Fig. 17 shows that correcting the FBT preparation with the transport prediction enhances the stationarity and controllability of this scenario. The primary and secondary X-points of the snowflake were maintained closer to their respective targets until the end of the discharge, holding the shape remarkably stationary for a longer time than the shots prepared with low- β_{pol} and low- $l_{i,3}$ but also than the reference shot #83575.

5 Conclusion and outlook

This paper presents the first results of a Kinetic Equilibrium Prediction for TCV full discharges, using RAPTOR for fast transport prediction and FBT for the inverse equilibrium, investigating the role of kinetic profiles in the feedforward coils programming and our ability to predict kinetic and current density profiles before the shot. These dis-

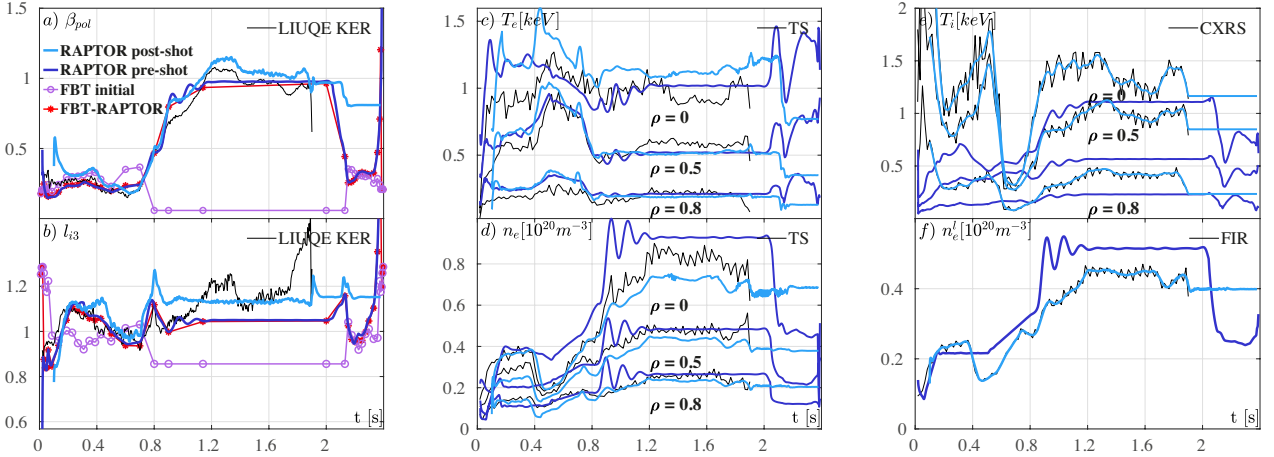


Figure 16: Overview of the KEP performed for TCV shot #83575. The pre-shot simulation (fully predictive without density measurements, dark blue) is compared to a post-shot simulation (light blue) using the same peaking and confinement factors but taking the line-averaged density and T_i from experiment. TS, CXRS and FIR data of shot #83575 are displayed in black in (c-f) as well as LIUQE-MER in (a-b). The coupling used an initial FBT run with a low β_{pol} and l_{i3} (in purple, a-b) used for the preparation of shot #83926 and the result after 2 iterations (in red) was used to prepare #83946, both shown in Fig. 17

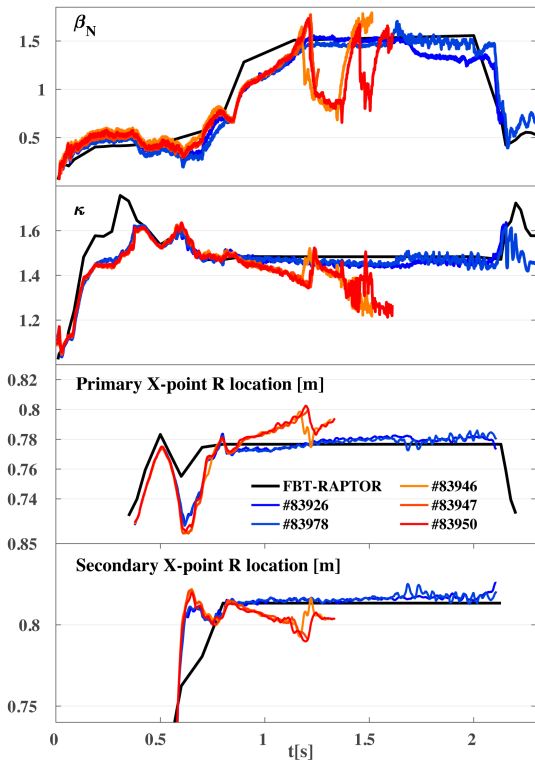


Figure 17: Evolution of β_N , elongation κ and X-point locations for upper NT plasmas with snowflake divertor configuration for a series of shots prepared with the same programming but different equilibrium preparation. Shots #[83946, 83947, 83950] (in red and orange), prepared with an initial FBT equilibrium with high β_{pol} and l_{i3} , and shots #[83926, 83978] (in blue), prepared with the FBT-RAPTOR corrections.

charges cover ramp-up, flat top and ramp-down phases, limited and diverted shape evolutions, L-

and H-mode phases, ohmic and NBI heating. TCV has 16 PF coils controlled by 16 independent power supplies, which allow to generate a large number of plasma shapes. The Martin scaling law [26] has been included in a new RAPTOR module and adapted to limited and unfavorable diverted configurations, automatically predicting the confinement mode and transitions during the simulation (Sec. 2.1). This H-mode prediction shows promising results in most of the cases studied (Sec. 3), and is mainly limited by the limited access to H-mode in high X-point height configurations and the role of radiation losses. The specific cases of near double-null shapes also need to be studied further and can provide insights to the L-H threshold evolution from favorable to unfavorable configurations. Despite the generally low level of core radiation in TCV plasma, modeling of impurity transport and line radiation using the already implemented ADAS cooling factors database [21, 91, 92], is envisioned in the future, for a refined estimation of the core profiles and power losses at the separatrix P_{sep} . The gradient-based model [19] is now extended to Negative Triangularity L-mode transport (Sec. 2.1). NT parameters which reproduce the best the set of simulated discharges (listed in Table 1), corroborate the H-mode like performances observed in NT plasmas [44]. Similarly, simulation of the ion heat transport has been included in the gradient-based model for the first time with RAPTOR over a wide range of discharges, and compared to a simple electron-to-ion data-driven scaling law (Sec. 2.1). We conclude that similar results can be obtained within the CXRS error-bars, provided that a total confinement factor is given that corresponds to the expected performance of the shot.

In Section 3, we show that, for a wide range of discharges, simulating from the pulse schedule and the experimental $n_{e,l}$ with a default set of parameters, including $H^{98(y,2)} = \{0.7, 1\}$ in PT L- and H-mode, is sufficient to predict the total ion and electron energy content within a 20% error-bars, with a good prediction of the L to H mode transition and of the overall kinetic profiles. The estimation of the line-averaged density from the gas programming has proven to be a crucial element of predict-first modeling. Its improvement, e.g. by using more advanced regression strategies or edge-to-core modeling, appears to be an important step toward the automatization and generalization of the prediction strategies presented in this work. However, we present a simple model for TCV that proved sufficient to design and test experimentally our predictions (Sec.4).

In Section 2.3, we show that internal profiles (p' , TT') obtained from the RAPTOR pre-shot simulations can help inform the Grad-Shafranov equation in the FBT inverse equilibrium solver. FBT is used before a discharge for preparing the plasma shape and feedforward PF coil currents and is usually parametrized with simple assumptions on the core profiles. We show that the FBT-RAPTOR coupling enables the integration of a more complex plasma dynamics while converging to a final solution within a few iterations and minutes, with a negligible systematic error between the two codes, hence a self-consistent solution is obtained with this loose coupling. Section 4 demonstrates the implementation of this new result in the TCV shot preparation system, by giving the new feedforward currents to the hybrid shape controller, facilitating the feedback control during the discharge. Experiments show that getting a better prediction of β_{pot} and l_{i3} and of the profiles can help improving the alignment of the shape and avoid vertical instabilities during the shot. In particular, the new coupling helped to better control a snowflake configuration with an upper NT plasma, maintaining the primary and secondary X-points close to their target until the end of the discharge. This kind of shape, known to be more difficult to control, proved to be more sensitive to the FBT-RAPTOR coupling than a standard PT-LSN configuration, for which the principle effect was a better alignment of the X-point target. Such physics-based results can then be used to inform a more advanced shape control model by providing better feedforward coil currents and dynamical profiles of the plasma.

We chose to have a loose coupling between FBT and RAPTOR, i.e. to compute equilibrium and transport separately, in order to facilitate its portability to the existing TCV shot preparation system, and given that transport calculations are only weakly dependent on the equilibrium. However, a tight coupling which would run RAPTOR, FBT and fast models for auxiliary heating and current-

drive systems, e.g. TORBEAM [93] for Electron Cyclotron Resonance Heating, RABBIT [60] for Neutral Beam Injection, at different time steps of a single run, could be of interest, as changes in heating and current sources have a stronger influence on the predicted plasma profiles. The gradient-based model, which assumes three regions of flat, stiff and pedestal gradients over the whole radius, can later be amended to include local changes in confinement, e.g. to include effects of the magnetic shear usually observed in advanced scenarios (as already done in other RAPTOR transport models [11]), or turbulence surrogate models like QLKNN [94] or TGLF-NN [95]. Finally, with the OH circuit equations already implemented in FBT, their integration into the KEP represents a natural extension of this work. This would allow the joint optimization of the plasma current induction together with the control of the plasma shape, thereby reducing the gap between the predicted and effective PF coil currents and enhancing both the precision and impact of the KEP in the preparation of TCV discharges.

Data availability

The simulation results presented in this article will be made available online in a public repository. They may be accessed and reused in accordance with the conditions specified in that repository.

Acknowledgments

This work has been carried out within the framework of the EUROfusion Consortium, partially funded by the European Union via the Euratom Research and Training Programme (Grant Agreement No 101052200 — EUROfusion). The Swiss contribution to this work has been funded in part by the Swiss State Secretariat for Education, Research and Innovation (SERI). Views and opinions expressed are however those of the author(s) only and do not necessarily reflect those of the European Union, the European Commission or SERI. Neither the European Union nor the European Commission nor SERI can be held responsible for them. This work was supported in part by the Swiss National Science Foundation.

ORCID iDs

C. E. Contré  0009-0008-3246-1860
A. Merle  0000-0003-1831-5644
O. Sauter  0000-0002-0099-6675
S. Van Mulders  0000-0003-3184-3361
R. Coosemans  0000-0001-8110-3156
G. Durr-Legoupil-Nicoud  0009-0002-5956-6482
F. Felici  0000-0001-7585-376X
O. Février  0000-0002-9290-7413
C. Heiss  0009-0005-9712-0643
B. Labit  0000-0002-0751-8182
A. Pau  0000-0002-7122-3346
Y. Poels  0000-0002-4071-4855

C. Venturini 0009-0005-9873-1171
 B. Vincent 0000-0001-5420-6002

Author contributions

C. E. Contré: Writing – review & editing, Writing – original draft, Investigation, Software, Conceptualization, Methodology, Visualization, Formal analysis; **A. Merle:** Writing – review & editing, Investigation, Methodology, Software; **O. Sauter:** Writing – review & editing, Supervision, Investigation, Conceptualization, Methodology, Formal analysis, Validation, Software; **S. Van Mulders:** Writing – review & editing, Conceptualization, Formal analysis, Software; **R. Coosemans:** Writing – review & editing, Formal analysis (ASTRA KER); **G. Durr-Legoupil-Nicoud:** Resources (NT-SF scenario); **F. Felici:** Writing – review & editing, Supervision, Software; **O. Février:** Resources (NT-SF scenario); **C. Heiss:** Visualization; **B. Labit :** Resources (PT-LSN scenario), Data curation (QCE); **A. Pau:** Writing – review & editing, Formal analysis (confinement state classification); **Y. Poels:** Formal analysis (confinement state classification); **C. Venturini:** Formal analysis (confinement state classification); **B. Vincent:** Writing – review & editing, Data curation (CXRS);

References

- [1] Ciattaglia S., Barabaschi P., Carretero J. A. *et al.* 2009 *Fusion Engineering and Design* **84** 2059–2063 ISSN 0920-3796
- [2] Hender T., Wesley J., Bialek J. *et al.* 2007 *Nuclear Fusion* **47** S128
- [3] Bandyopadhyay I., Igochine V., Sauter O. *et al.* 2025 *Nuclear Fusion* **65** 103001 ISSN 0029-5515 publisher: IOP Publishing
- [4] Giacomini M., Pau A., Ricci P. *et al.* 2022 *Physical Review Letters* **128** 185003
- [5] Artaud J., Imbeaux F., Garcia J. *et al.* 2018 *Nuclear Fusion* **58** 105001 ISSN 0029-5515, 1741-4326
- [6] Lyons B. C., McClenaghan J., Slendebroek T. *et al.* 2023 *Physics of Plasmas* **30** 092510 ISSN 1070-664X
- [7] Luda T., Angioni C., Dunne M. *et al.* 2021 *Nuclear Fusion* **61** 126048 ISSN 0029-5515, 1741-4326
- [8] Romanelli M., Corrigan G., Parail V. *et al.* 2014 *Plasma and Fusion Research* **9**
- [9] Janky F., Fable E., Englberger M. 2021 *Fusion Engineering and Design* **163** 112126 ISSN 0920-3796
- [10] Hofmann F., Lister J. B., Anton W. *et al.* 1994 *Plasma Physics and Controlled Fusion* **36** B277
- [11] Felici F., Sauter O., Coda S. *et al.* 2011 *Nuclear Fusion* **51** 083052 ISSN 0029-5515 publisher: IOP Publishing
- [12] Hofmann F. 1988 *Computer Physics Communications* **48** 207–221 ISSN 0010-4655
- [13] Felici F., Citrin J., Teplukhina A. A. *et al.* 2018 *Nuclear Fusion* **58** 096006 ISSN 0029-5515 publisher: IOP Publishing
- [14] Carpanese F., Felici F., Galperti C. *et al.* 2020 *Nuclear Fusion* **60** 066020 ISSN 0029-5515 publisher: IOP Publishing
- [15] Piron C., Manduchi G., Bettini P. *et al.* 2017 *Fusion Engineering and Design* **123** 616–619 ISSN 0920-3796
- [16] Piron C., Felici F., Faugeras B. *et al.* 2021 *Fusion Engineering and Design* **169** 112431 ISSN 0920-3796
- [17] Kudlacek O., David P., Gómez Ortiz I. *et al.* 2024 *Nuclear Fusion* **64**
- [18] Reisner M., Contré C., Felici F. *et al.* 2026 *Fusion Engineering and Design* **222** 115474 ISSN 0920-3796
- [19] Teplukhina A., Sauter O., Felici F. 2017 *Plasma Physics and Controlled Fusion* **59**
- [20] Van Mulders S., Felici F., Sauter O. *et al.* 2021 *Nuclear Fusion* ISSN 0029-5515
- [21] Van Mulders S., Sauter O., Contré C. *et al.* 2023 *Plasma Physics and Controlled Fusion* **66**
- [22] Van Mulders S., Sauter O., Contré C. *et al.* 2023 *Plasma Physics and Controlled Fusion* **66**
- [23] Van Mulders S., Sauter O., Bock A. *et al.* 2024 *Nuclear Fusion* **64** 026021 ISSN 0029-5515, 1741-4326
- [24] van de Plassche K. L., Citrin J., Bourdelle C. *et al.* 2020 *Physics of Plasmas* **27** 022310 ISSN 1070-664X publisher: American Institute of Physics
- [25] Kim D., Merle A., Sauter O. 2016 *Plasma Physics and Controlled Fusion* **58** 055002 ISSN 0741-3335, 1361-6587
- [26] Martin Y. R., Takizuka T. and Group T. I. C. H.-m. T. D. 2008 *Journal of Physics: Conference Series* **123** 012033 ISSN 1742-6596 11th IAEA Technical Meeting on H-mode Physics and Transport Barrier
- [27] Moret J.-M., Duval B., Le H. *et al.* 2015 *Fusion Engineering and Design* **91**
- [28] Van Mulders S., McIntosh S., Carpanese F. *et al.* 2026 *Nuclear Fusion* **66** 026026 ISSN 0029-5515

- [29] Carpanese F. 2021 *Development of free-boundary equilibrium and transport solvers for simulation and real-time interpretation of tokamak experiments* PhD Thesis EPFL Lausanne
- [30] Mc Carthy P. J. 1999 *Physics of Plasmas* **6** 3554–3560 ISSN 1070-664X
- [31] R. Fischer, J. C. F., B. K. 2010 *Fusion Science and Technology* **58** 675–684 ISSN 1536-1055 _eprint: <https://doi.org/10.13182/FST10-110>
- [32] Fischer R., Giannone L., Illerhaus J. 2020 *Fusion Science and Technology* **76** 1–15
- [33] Lao L., St. John H., Stambaugh R. 1985 *Nuclear Fusion* **25** 1611 ISSN 0029-5515
- [34] Xing Z. A., Eldon D., Nelson A. O. *et al.* 2021 *Fusion Engineering and Design* **163** 112163 ISSN 0920-3796
- [35] Ostuni V., Morales J., Artaud J.-F. *et al.* 2022 *Nuclear Fusion* **62** 106034 ISSN 0029-5515 publisher: IOP Publishing
- [36] Heumann H., Blum J., Boulbe C. *et al.* 2015 *Journal of Plasma Physics* **81** 905810301 ISSN 0022-3778, 1469-7807
- [37] Battaglia J., Teplukhina A., Wai J. 2025 Pulse preparation workflows for sparc plasma operations Oral presentation 67th Annual Meeting of the APS Division of Plasma Physics (DPP), Long Beach, California
- [38] Felici F., Merle A., Wai J. 2025 Tokamak scenario planning and simulation including the plasma startup phase using the meq suite of codes with application to tcv, sparc and arc Oral presentation 67th Annual Meeting of the APS Division of Plasma Physics (DPP), Long Beach, California
- [39] Citrin J., Goodfellow I., Raju A. *et al.* 2024 TORAX: A Fast and Differentiable Tokamak Transport Simulator in JAX arXiv:2406.06718 [physics]
- [40] Wai J. T., Boyer M. D., Battaglia D. J. *et al.* 2025 Feedforward equilibrium trajectory optimization with GSPulse arXiv:2506.21760 [physics]
- [41] Coda S., Merle A., Sauter O. *et al.* 2021 *Plasma Physics and Controlled Fusion* **64**
- [42] Marinoni A., Sauter O. and Coda S. 2021 *Reviews of Modern Plasma Physics* **5** 6
- [43] Thome K. E., Austin M. E., Hyatt A. *et al.* 2024 *Plasma Physics and Controlled Fusion* **66** 105018 ISSN 0741-3335 publisher: IOP Publishing
- [44] Mariani A., Aucone L., Balestri A. *et al.* 2024 *Nuclear Fusion* **64** 106024 ISSN 0029-5515 publisher: IOP Publishing
- [45] Sauter O., Hong R., Marinoni A. *et al.* 2025 *Plasma Physics and Controlled Fusion* **67** 075009
- [46] Teplukhina A. 2018 *Realistic multi-machine tokamak profile simulations and numerical ramp-down optimization using the RAPTOR code* Ph.D. thesis EPFL Lausanne
- [47] Van Mulders S. 2023 *Full-discharge simulation and optimization with the RAPTOR code, from present tokamaks to ITER and DEMO* Ph.D. thesis EPFL Lausanne
- [48] Sauter O. and Medvedev S. Y. 2013 *Computer Physics Communications* **184** 293–302 ISSN 0010-4655
- [49] Hinton F. L. and Hazeltine R. D. 1976 *Reviews of Modern Physics* **48** 239–308 publisher: American Physical Society
- [50] Felici F. 2011 *Real-Time Control of Tokamak Plasmas: from Control of Physics to Physics-Based Control* Ph.D. thesis EPFL Lausanne
- [51] Erba M., Aniel T., Basiuk V. 1998 *Nuclear Fusion* **38** 1013 ISSN 0029-5515
- [52] Citrin J., Breton S., Felici F. *et al.* 2015 *Nuclear Fusion* **55** 092001 ISSN 0029-5515 publisher: IOP Publishing
- [53] Geiger B., Karpushov A. N., Duval B. P. *et al.* 2017 *Plasma Physics and Controlled Fusion* **59** 115002 ISSN 0741-3335 publisher: IOP Publishing
- [54] Confinement I. P. E. G. o., Transport, Modelling I. P. E. G. o. C. 1999 *Nuclear Fusion* **39** 2175 ISSN 0029-5515
- [55] Ryter F., Stober J., Stähler A. *et al.* 2001 *Nuclear Fusion* **41** 537–550 ISSN 0029-5515
- [56] Garbet X., Mantica P., Angioni C. *et al.* 2004 *Plasma Physics and Controlled Fusion* **46** B557 ISSN 0741-3335
- [57] Doyle E., Houlberg W., Kamada Y. 2007 Chapter 2: Plasma confinement and transport - IOPscience
- [58] Sauter O., Brunner S., Kim D. *et al.* 2014 *Physics of Plasmas* **21** 055906 ISSN 1070-664X publisher: American Institute of Physics
- [59] Garbet X., Mantica P., Ryter F. *et al.* 2004 *Plasma Physics and Controlled Fusion* **46** 1351–1373 ISSN 0741-3335, 1361-6587

- [60] Weiland M., Bilato R., Dux R. *et al.* 2018 *Nuclear Fusion* **58** 082032 ISSN 0029-5515 publisher: IOP Publishing
- [61] Labit B., Bagnato P., Duval B. P. *et al.* 2025 *Plasma Physics and Controlled Fusion* **67** 055010 ISSN 0741-3335 publisher: IOP Publishing
- [62] Hinton F. L. 1985 *Nuclear Fusion* **25** 1457 ISSN 0029-5515
- [63] Wagner F., Bartiromo R., Becker G. *et al.* 1985 *Nuclear Fusion* **25** 1490 ISSN 0029-5515
- [64] ASDEX-team 1989 *Nuclear Fusion* **29** 1959 ISSN 0029-5515
- [65] Meyer H., Field A. R., Akers R. J. *et al.* 2004 *Plasma Physics and Controlled Fusion* **46** A291 ISSN 0741-3335
- [66] Meyer H., Carolan P. G., Conway G. D. *et al.* 2005 *Nuclear Fusion* **46** 64 ISSN 0029-5515
- [67] Faitsch M., Eich T., Harrer G. *et al.* 2021 *Nuclear Materials and Energy* **26** 100890 ISSN 2352-1791
- [68] Nelson A., Paz-Soldan C. and Saarelma S. 2022 *Nuclear Fusion* **62** 096020 ISSN 0029-5515
- [69] Nelson A. 2023 *Physical Review Letters* **131**
- [70] Sauter O., Bagnato F., Balestri A. *et al.* 2023 Negative triangularity tokamak operation in tcv 29th IAEA Fusion Energy Conference, London, 2023, paper IAEA-EX-P-27781
- [71] Lütjens H., Bondeson A. and Sauter O. 1996 *Computer Physics Communications* **97** 219–260 ISSN 00104655
- [72] Wilson H. S., Nelson A. O., McClenaghan J. *et al.* 2024 *Plasma Physics and Controlled Fusion* **67** 015026 ISSN 0741-3335
- [73] Grad H. and Rubin H. 1958 *Proceedings of the 2nd United Nations International Conference on the Peaceful Uses of Atomic Energy* vol 31 (Geneva: UN) p. 190
- [74] Shafranov V. D. 1958 *Soviet Phys. JETP* **Vol: 6** institution: Academy of Sciences, USSR
- [75] Sauter O. and Medvedev S. 2013 *Computer Physics Communications* **184** 293–302 ISSN 0010-4655
- [76] Mukhovatov V. S. and Shafranov V. D. 1971 *Nuclear Fusion* **11** 605–633 ISSN 0029-5515
- [77] Marchioni S. 2024 *Vertical Instability Studies in the TCV Tokamak and Development and Application of Multimachine Real-Time Proximity Control Strategies* Ph.D. thesis EPFL
- [78] Jackson G., Casper T., Luce T. *et al.* 2008 *Nuclear Fusion* **48** 125002 ISSN 0029-5515
- [79] Zakharov L. E. and Shafranov V. D. 1986 Equilibrium of Current-Carrying Plasmas in Toroidal Configurations *Reviews of Plasma Physics, Volume 11.* vol 11 ed Leontovich M. A. p 153
- [80] Guizzo S., Nelson A. O., Hansen C. 2024 *Plasma Physics and Controlled Fusion* **66** 065018 ISSN 0741-3335 publisher: IOP Publishing
- [81] Poels Y., Venturini C., Pau A. *et al.* 2025 *Nuclear Fusion* **65** 096022
- [82] Pau A., Sauter O., Sommariva C. *et al.* 2023 A modern framework to support disruption studies: the EUROfusion disruption database
- [83] Andrew Y., Hawkes N. C., O’Mullane M. G. *et al.* 2004 *Plasma Physics and Controlled Fusion* **46** A87 ISSN 0741-3335
- [84] Scaggion A., Martin Y., Reimerdes H. 2012 H-mode access with different x-point height in tcv vol 36F p P2.093 ISBN 2-914771-79-7 meeting Name: 39th EPS Conference on Plasma Physics and 16th International Congress on Plasma Physics
- [85] Razumova K. A., Andreev V. F., Dnestrovskij A. Y. *et al.* 2008 *Plasma Physics and Controlled Fusion* **50** 105004 ISSN 0741-3335
- [86] Wágner D., Fable E., Pitzschke A. *et al.* 2012 *Plasma Physics and Controlled Fusion* **54** 085018 ISSN 0741-3335 publisher: IOP Publishing
- [87] Perek A., Vijvers W. a. J., Andrebe Y. *et al.* 2019 *Review of Scientific Instruments* **90** ISSN 0034-6748 publisher: AIP Publishing
- [88] Pustovitov V. D. 2001 *Nuclear Fusion* **41** 721 ISSN 0029-5515
- [89] Février O., Durr-Legoupil-Nicoud G., Contré C. *et al.* 2025 Core-edge integration studies in negative triangularity in tcv
- [90] Pesamosca F., Felici F., Coda S. 2022 *Fusion Science and Technology* **78** 427–448 ISSN 1536-1055, 1943-7641 publisher: American Nuclear Society _eprint: <https://doi.org/10.1080/15361055.2022.2043511>
- [91] Atomic Data and Analysis Structure ({ADAS})
- [92] Maget P., Manas P., Artaud J.-F. *et al.* 2022 *Plasma Physics and Controlled Fusion* **64** 045016 ISSN 0741-3335 publisher: IOP Publishing

- [93] Poli E., Bock A., Lochbrunner M. *et al.* 2018
Computer Physics Communications **225** 36–46
ISSN 0010-4655
- [94] Fransson E., Gillgren A., Ho A. *et al.* 2023
Physics of Plasmas **30** 123904 ISSN 1070-664X
- [95] Cao Y., Zhang F., Liu W. *et al.* 2025 Tglf-sinn:
Deep learning surrogate model for accelerating
turbulent transport modeling in fusion
- [96] Sheikh U. A., Simons L., Duval B. P. *et al.*
2022 *Review of Scientific Instruments* **93**
113513 ISSN 0034-6748

A Additional figures

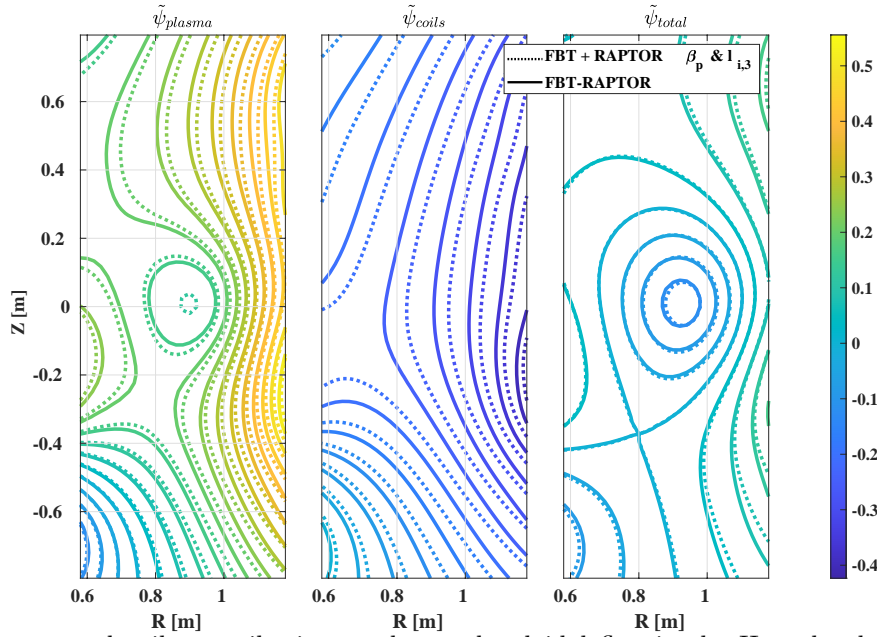


Figure A.1: Plasma and coils contribution to the total poloidal flux in the H-mode phase ($t = 1.3s$) of #81882 centered around the total flux at the plasma boundary, $\tilde{\psi} = \psi - \psi_B$. The full profile coupling (solid line) is compared to constraining β_{pol} and q_A from RAPTOR in the initial FBT calculation and keeping the same value of I_p (in dotted line), showing non negligible differences in plasma flux surfaces and PF coils flux generation

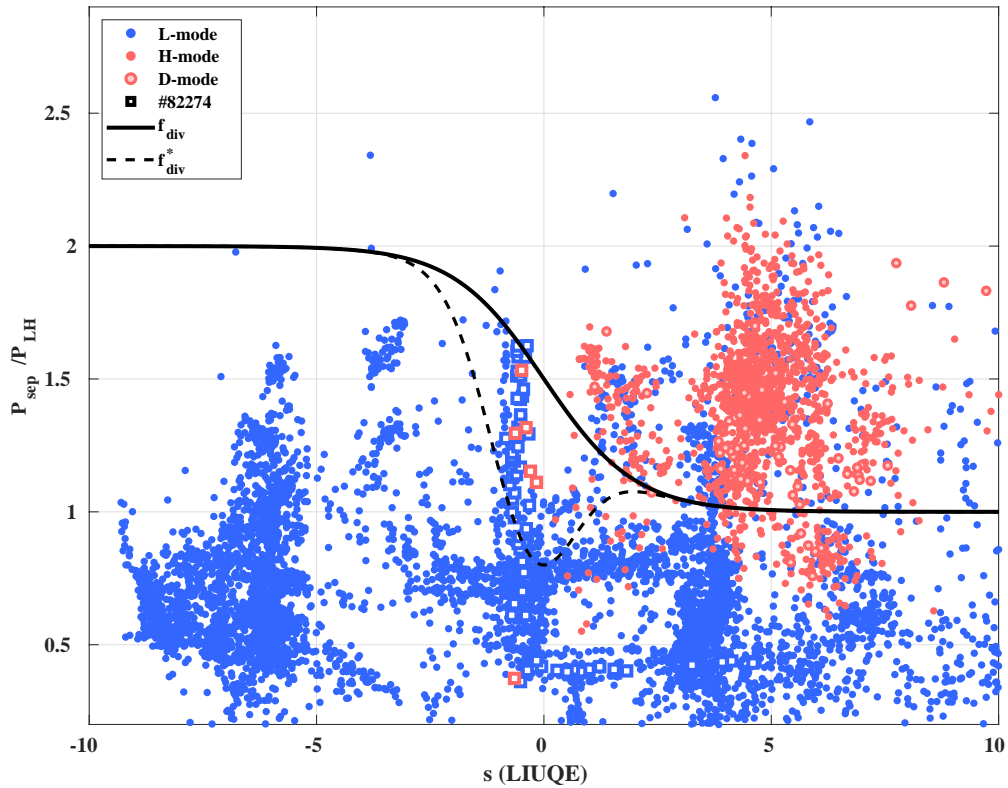


Figure A.2: Alternative version of Figure 11 accounting for core radiation in the computation of $P_{sep} = P_{oh} + P_{aux} - P_{rad,core}$, from the RADCAM tomographic inversion [96]. Each point corresponds to a time sample from 175 experiments having a diverted configuration, showing the dependence of the confinement state on the P_{sep}/P_{LH} ratio and the s value (reconstructed with LIUQE). The f_{div} function is the same as used in simulations and in Fig. 11.

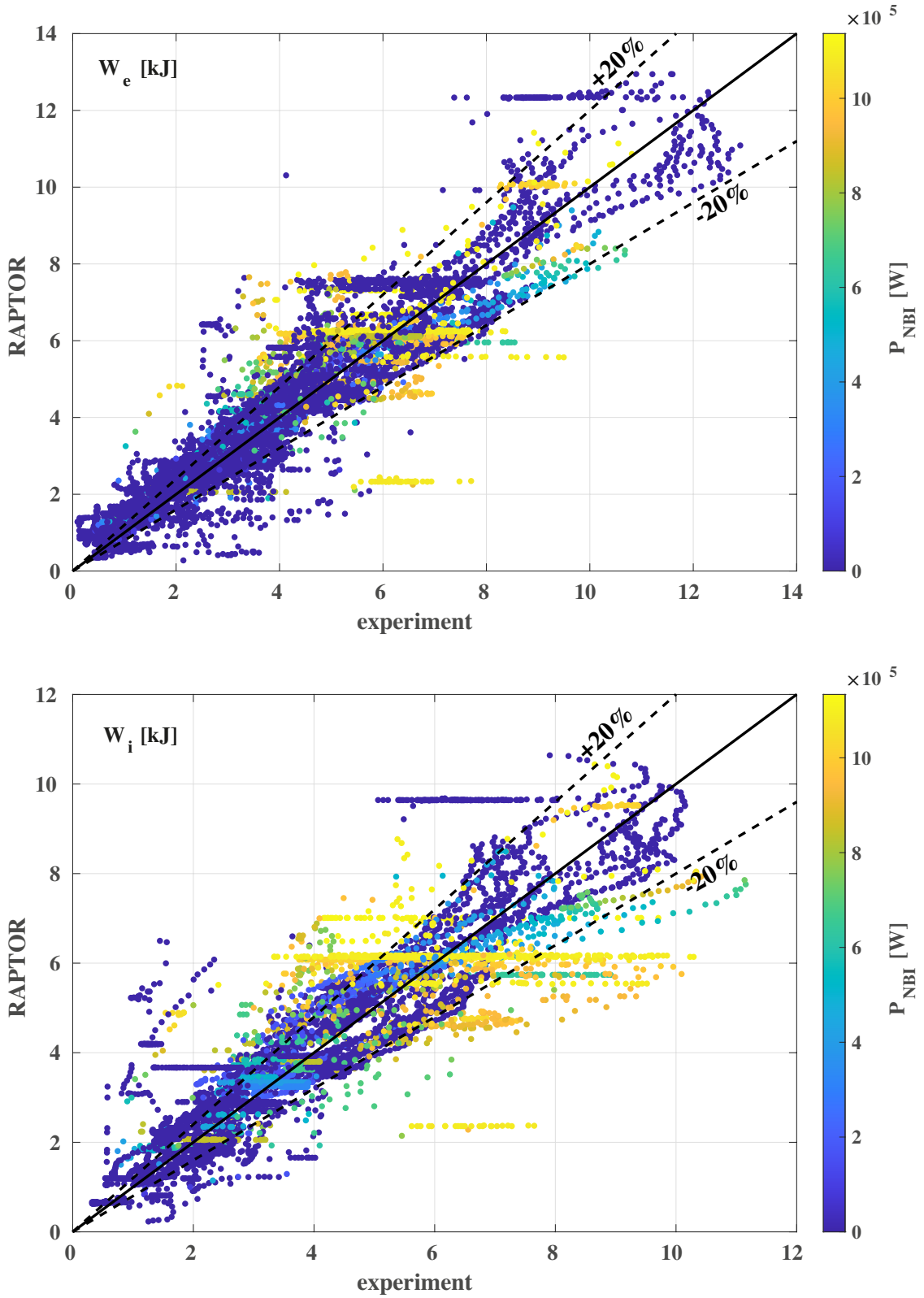


Figure A.3: Comparison of W_e and W_i predicted by RAPTOR with values reconstructed from experiments for, respectively, 211 shots with TS and 160 shots with CXRS measurements, at every measurement time instants. The dashed lines correspond to $W_{e,i}^{\text{experiment}} \pm 20\%$. RAPTOR predictions were made from only the pulse schedule, predicting $n_{e,l}$ from the gas references and solving for T_i .

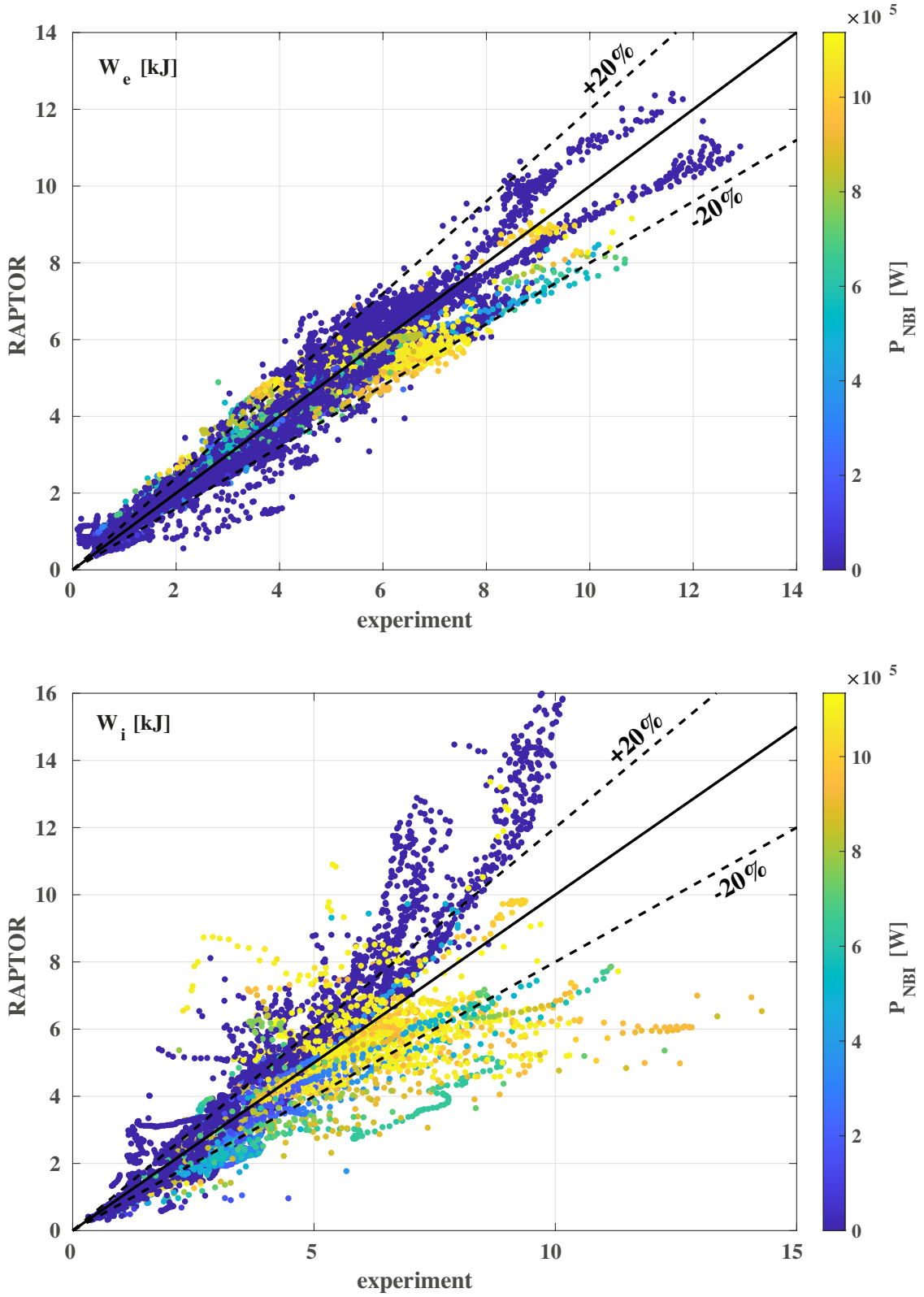


Figure A.4: Comparison of W_e and W_i predicted by RAPTOR with values reconstructed from experiments for, respectively, 206 shots with TS and 156 shots with CXRS measurements, at every measurement time instants. The dashed lines correspond to $W_{e,i}^{\text{experiment}} \pm 20\%$. RAPTOR predictions were made from the pulse schedule, using the experimental $n_{e,l}$ and the electron-to-ion scaling in Eq. 2.5.